Composite Structures 279 (2022) 114779

Contents lists available at ScienceDirect

Composite Structures

journal homepage: www.elsevier.com/locate/compstruct

Confinement model for LRS FRP-confined concrete using conventional regression and artificial neural network techniques

Haytham F. Isleem [a], Feng Peng [a,*], Bassam A. Tayeh [b]

[a] Postdoctoral Researcher, Department of Civil Engineering, Tsinghua University, Beijing, China
[b] Civil Engineering Department, Faculty of Engineering, Islamic University of Gaza, P.O. Box 108, Gaza Strip, Palestine

ARTICLE INFO

Keywords:
Fiber-reinforced polymer (FRP)
Concrete
Strength
Artificial neural networks (ANN)
Axial stress–strain response

ABSTRACT

Concrete confined using fiber-reinforced polymer (FRP) composites experience significant enhancements in strength and strain. For the seismic retrofitting of existing reinforced concrete (RC) structures, a large rupture strain (LRS) FRP (i.e., polyethylene terephthalate and naphthalate, denoted as PET and PEN respectively), with a larger rupture strain of more than 5%, is a promising alternative to conventional FRPs with a rupture strain of less than 3%. The majority of analytical models on the stress–strain behavior of FRP-confined concrete under axial compression have focused largely on concrete confined with the traditional FRP material. Analytical research on LRS FRP-confined concrete is, however, limited. Moreover, all existed stress–strain models were determined based on theoretical analysis and test data fitting. In this paper, the artificial neural networks (ANN) method is employed to build a confinement model directly from experimental data to predict the different components of the stress–strain response. A test database consisting of 226 axial compression tests on LRS FRP-confined concrete specimens is used. The test results, in terms of full confined stress–strain response, strength, strain, FRP rupture strain, and dilation response were investigated. Predictive expressions and practical ANN models for the strength, strain, and shape of an axial stress–strain response are provided. Existing models for LRS FRP-confined concrete were also evaluated. The results of the existing and proposed models report that the proposed methods achieve significantly better results.

1. Introduction

A large number of experimental and analytical investigations have been conducted to understand and simulate the compressive behavior of fiber-reinforced polymer (FRP) confined concrete, and as a result, axial stress–strain models have been provided. The use of FRP confined concrete columns has been proven in enhancing the strength and ductility of FRP confined concrete columns [i.e., [1–30,79,81,82]]. The compressive behavior of FRP-confined concrete is controlled by both the mechanical and geometric properties. The evidence from existing laboratory tests has demonstrated the effects of several important factors such as the cross-sectional size and shape, the corner radius of the column cross-section, the compressive strength of unconfined concrete, the amount of FRP confinement, the FRP elastic modulus, and the amount of internal steel hoop reinforcement.

FRP materials that have been used in seismic strengthening and retrofitting of reinforced concrete (RC) structures can be classified into two types based on the elastic modulus and its rupture strain: FRPs with high elastic modulus but low rupture strain, and FRPs with low elastic modulus but large rupture strain. The traditional FRPs, which are most widely used, include Carbon FRP (CFRP), Glass FRP (GFRP), and Aramid FRP (AFRP). The majority of tests and models available in the literature are based on traditional FRPs. The newly developed LRS FRP materials which include Polyethylene Naphthalate (PEN FRP) and Polyethylene Terephthalate FRP (PET FRP) have drawn researchers' attention compared with traditional FRP materials.

For the seismic strengthening and retrofitting of reinforced concrete (RC) structures, in which ductility enhancement is of major importance, LRS FRPs can provide a more ductile behavior with almost the same level of strength enhancement [29]. Generally, the low elastic modulus of these materials can be compensated by the use of a thicker LRS FRP jacket. Therefore, only a limited number of experimental tests have been conducted, to date, that consider such material [i.e., [31–44]], and as a result, very limited stress–strain models has been developed based on confinement by LRS FRP composite materials [i.e., [43–45]].

Although many models for FRP confined concrete have been proposed, they may not be suitable for LRS FRP confined concrete. Dai et al.

* Corresponding author.
E-mail addresses: haythamisleem@hit.edu.cn (H.F. Isleem), fengpeng@tsinghua.edu.cn (F. Peng), btayeh@iugaza.edu.ps (B.A. Tayeh).

https://doi.org/10.1016/j.compstruct.2021.114779
Received 16 May 2021; Received in revised form 19 September 2021; Accepted 5 October 2021
Available online 9 October 2021

Abbreviations

E_c	elastic modulus of unconfined concrete (MPa)
E_{frp1}	initial secant modulus of a fiber-reinforced polymer material (MPa)
E_{frp2}	second secant modulus of a fiber-reinforced polymer material (MPa)
E^*_{frp}	effective secant modulus of FRP wraps in the hoop direction (MPa)
f'_c	cylinder compressive strength of unconfined concrete (MPa)
ε_{co}	strain corresponding to the compressive strength of unconfined concrete cylinder (mm/mm)
f_{cc}	peak axial compressive strength of FRP-confined concrete (MPa)
ε_{cc}	strain corresponding tof_{cc}(mm/mm)
f_{cu}	axial compressive strength at FRP failure (MPa)
ε_{cu}	strain corresponding tof_{cu}(mm/mm)
ε_l	hoop strain of FRP-confined concrete (mm/mm)
σ_l	lateral confining stress of the FRP wraps (MPa)
A_e	effectively confined concrete area of a cross-section (mm^2)
A_g	gross cross-section concrete area (mm^2)
b	width of a rectangular cross-section (mm)
h	depth of a rectangular cross-section (mm)
l	height of a specimen (mm)
d_e	the equivalent diameter of a rectangular cross-section (mm)
f_{frp}	ultimate tensile strength of fiber-reinforced polymer material (MPa)
$f_{lf,o}$	nominal lateral confining stress of FRP wraps ($f_{lf,o} = K_{lf}\varepsilon_{frp}$) (MPa)
$f_{lf,a}$	lateral confining stress of the FRP wraps at failure ($f_{lf,a} = K_{lf}\varepsilon_{h,rup}$) (MPa)
K_{lf}	lateral confining stiffness of FRP wraps (MPa)
r_c	corner radius of a non-circular cross-section (mm)
n_{frp}	total number of layers of FRP wraps
t_{frp}	thickness of a single layer of FRP composite material (mm)
$\varepsilon_{h,rup}$	failure hoop rupture strain of the FRP wraps (mm/mm)
$k_{\varepsilon,frp}$	reduction factor for FRP hoop strain
ε_{frp0}	strain of fiber-reinforced polymer material at the intersection between the first and second stress-strain segments (mm/mm)
ε_{frp}	strain of fiber-reinforced polymer material at testing failure (mm/mm)
D	diameter of a circular cross-section (mm)
K^*_{lf}	proposed threshold lateral confining pressure of the FRP wraps (MPa)
f_{ls}	lateral confining stiffness of the internal steel ties (MPa)
σ_c	axial compressive stress (MPa)
ε_c	strain corresponding to σ_c (mm/mm)
s	the center-to-center spacing between two adjacent steel stirrups (mm)
ν_s	secant Poisson's ratio of concrete
ν_i	initial Poisson's ratio of concrete
ρ_s	ratio of longitudinal steel reinforcement
$\rho_{ls,x}$	ratio of hoop steel reinforcement in the x-direction
$\rho_{ls,y}$	ratio of hoop steel reinforcement in the y-direction
$A_{ls,x}$	cross-section area of hoop steel reinforcement along x-direction (mm^2)
$A_{ls,y}$	cross-section area of hoop steel reinforcement along y-direction (mm^2)
f_{yh}	yield strength of hoop steel reinforcement (MPa)
f_{yv}	yield strength of vertical steel reinforcement (MPa)
ρ^*_{ls}	equivalent volumetric ratio of internal steel ties
ρ_{frp}	volumetric ratio of FRP wraps
E_{co}	secant modulus at the peak condition of unconfined concrete (MPa)
r	parameter for the overall shape of a stress-strain response

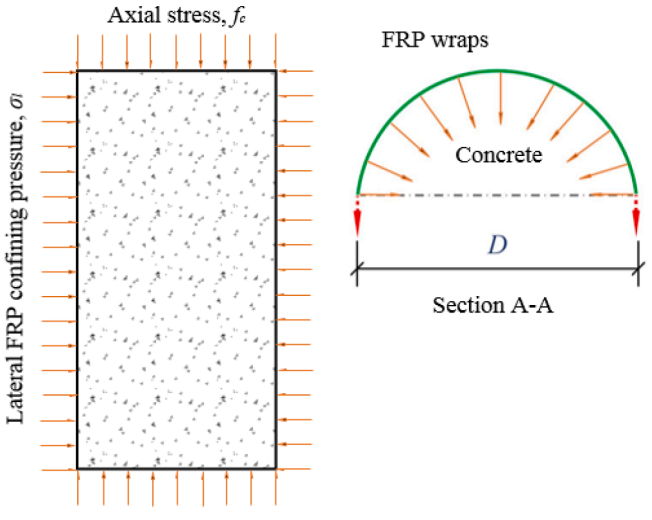

Fig. 1. Full confinement mechanism in FRP confined circular concrete columns (i.e.,D is the diameter of a circular concrete core, mm; $\sigma_l$is lateral confining stress of the FRP wraps, MPa).

[29] found that the existing models are unable to predict the ultimate deformation capacity of concrete cylinders confined with PET and PEN FPR. Based on the existing models, they suggested an axial compression stress–strain model with a new axial strain versus lateral strain relationship, which can well capture the softening and hardening behaviors of both conventional and LRS FRP-confined concrete. This model was further improved by Bai et al. [30] based on updated test results. The combined use of CFRP or GFRP and PET FRP for confining concrete was studied by Ispir et al. [31], and an energy balance approach was used to predict the key features of the stress–strain response. Dang et al. [80] investigated ductile concrete confined with FRP. Zeng et al. [32] conducted tests on normal, high- and ultra-high-strength concrete confined with LRS FRP. A unified design-oriented stress–strain model was then proposed.

These models for FRP-confined unreinforced concrete in circular cross-sections can be interpreted in 3D coordinate [76,77]; the concrete dilates uniformly in the lateral direction, hence it receives uniform confining stress from the FRP (see Fig. 1) and the concrete's damage, using a concrete damage plasticity model into finite element software ABAQUS 6.14, is uniformly distributed around the cross-section as evident from Fig. 2a. Unlike circular columns, weak or ineffective confinement usually occurs in non-circular sections or circular sectioned columns with a limited amount of confinement. The effectiveness of confinement around the cross-section is highly non-uniform in the case of a rectangular cross-section (Figs. 2 and 3) and varies with the variation of the section side length. According to existing tests, concrete

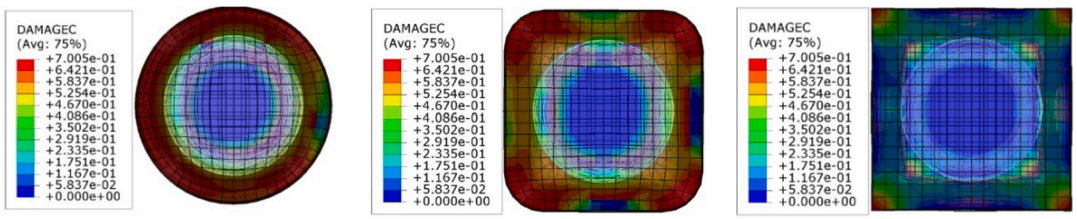

Fig. 2. Stress variation around FRP-confined concrete columns with different corner radii. *Note:* (a) is a control specimen from Ref. [75], and columns in Figs. (b and c) are currently proposed geometries with the same FRP material and reinforcement configuration.

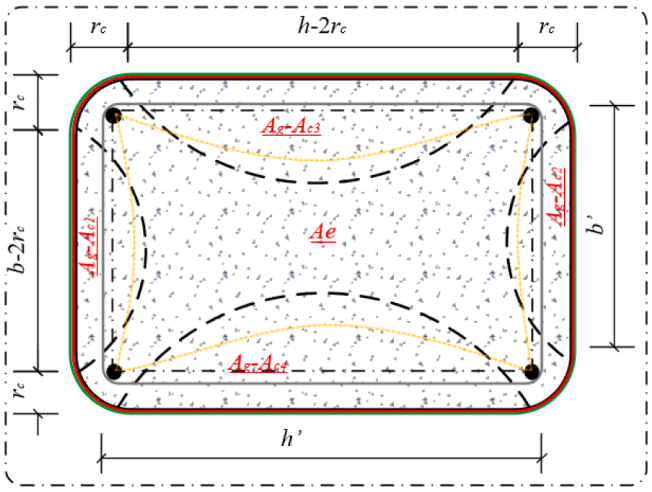

Fig. 3. Full confinement mechanism in FRP confined rectangular concrete columns (where r_c is the corner radius of a non-circular cross-section, mm; b and h are the width and depth of a rectangular cross-section, respectively; A_e is effectively confined concrete area of a cross-section, mm^2).

dilation is higher in the short direction as a result of the reduced effectiveness of FRP confinement due to experiencing a considerable bending deformation along its long side [i.e., [26–30]]. In non-circular columns, there is a stress concentration around the confined concrete core at the corner locations which acts like a knife, i.e., particularly for a case of sharp corners as evident from Fig. 2c, and prematurely ruptures the FRP wraps resulting in reduced effectively confined concrete. As a result, the stress–strain responses exhibit a strength softening region after reaching the peak stress level [i.e., [1–8]].

For non-circular columns, Saleem et al. [33] found that the confinement of PET FRP reduces as the cross-sectional aspect ratio increases and increases with increasing the corner radius. When the cross-sectional shape changes from circular to noncircular, the stress–strain response changes from a bilinear shape to a tri-linear shape with a significant strength softening in its second region. It was also observed that the use of LRS FRPs can efficiently delay the premature rupture of FRP at sharp corners. Saleem et al. [34] further pointed out that few of the existing models can accurately predict the ultimate strength and strain of PET FRP-confined concrete in square and rectangular cross-sections. Based on their findings, a new model was developed for PET FRP-confined concrete specimens with circular and noncircular sections [34].

In RC columns, the effectiveness of confinement of FRP is usually limited by the buckling of longitudinal steel bars. Using commercial finite element software, three FRP-RC columns tested by AlAjarmeh et al. [75] with different FRP hoop configurations and exhibited different failure modes were simulated in this paper based on excellent calibration with the tests. The results show that reducing the spacing of the lateral reinforcing bars improved the efficiency of concrete-core confinement and the longitudinal bars until failure. It is clearly seen that for columns without FRP confinement (Fig. 4a) the PEEQ value of about 0.110 (material's inelastic deformation) is higher than those of columns with FRP confinement (i.e., PEEQ value = 0.058; hoop spacing = 50 mm in Fig. 4b). The larger FRP hoop spacing reveals greater buckling and deformation. This situation is even more critical in noncircular columns where the FRP ruptures due to a combination of buckling of the steel reinforcement bars and stress concentrations at the corners. In recent years, Saleem et al. [35] have studied the influence of internal steel reinforcement on the axial compressive behavior of square and rectangular RC column specimens confined with LRS PET FRPs. The parameters that are experimentally investigated are the number of PET FRP layers, the spacing of internal hoop reinforcement, and the aspect ratio of cross-sections. Several important conclusions were drawn from

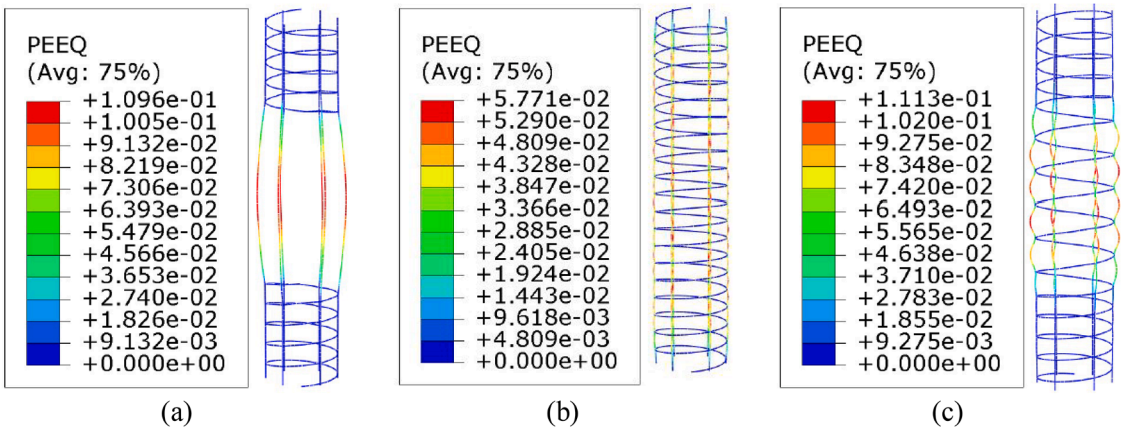

Fig. 4. FEM failure characteristics of tests reported in Ref. [75]: (a) Tested column without FRP confinement; (b) Column with 50 mm spiral spacing; (c) Column with 100 mm spiral spacing.

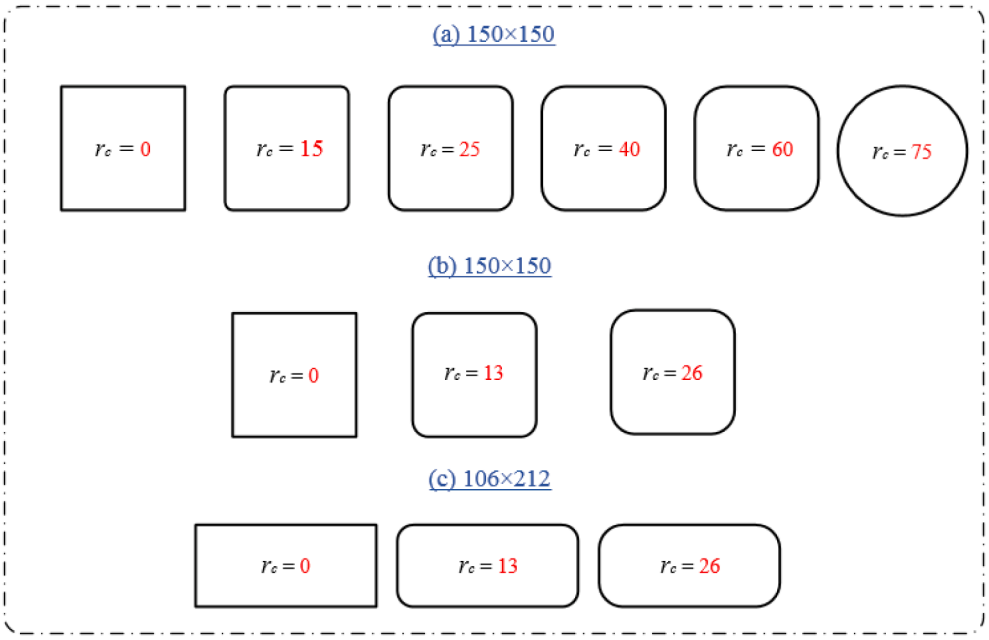

Fig. 5. Corner radius variations: (a) Tested specimens from Han et al. [36]; (b & c) Tested specimens from Saleem et al. [33,35].

the results of the tested specimens. In general, the specimens exhibited full strain hardening or post-peak softening and subsequent flat or ascending response behaviors mainly depending on the variation of test parameters. For example, the stress–strain response of specimens with light to medium amount of confinement exhibited a slight strength softening and a horizontal flat plateau up to FRP rupture, whereas for specimens with medium to a high level of confinement, a slight strength hardening was observed in the stress–strain curve. Only for greater effectiveness of confinement, the tested response after the second zone was ascending.

To date, all the available confinement models about LRS FRP-confined concrete in literature has not considered the effect of internal steel hoop reinforcing bars on its axial compression behavior [i.e., [30]], with few models to account for the effects have been provided only for concrete specimens with conventional FRP composite wraps [i.e., [1–8]. One of the challenges that usually face the designers is to accurately estimate the compressive strength and strain of FRP-confined RC columns at failure. This can be achieved using destructive methods through laboratory tests or non-destructive methods such as analytical design models. A full stress–strain model under monotonic loading as an envelope response of the cyclic model is also required for the seismic analysis of FRP-confined RC columns based on fiber model [i.e., [46] or finite-element analysis [i.e., [47,48].

Recently, researchers have used the power of advanced learning techniques in civil engineering systems [i.e., [49–63,78]], and several studies to successfully estimate the properties of confined concrete have been provided [i.e., [44–55]]. Among these studies, Only Oreta and Kawashima [46] have explored the application of artificial neural networks (ANN) to predict the axial compressive strength and strain of steel-confined circular concrete columns. An ANN model with input variables, which include the unconfined concrete compressive strength, the concrete core diameter, the height of specimen, the longitudinal steel ratio, and the confinement pressure by the hoop reinforcement was provided. When the input data are limited, the ANN models are shown to be significantly important in simulating physical processes. The ANN model was also found to perform better compared with some Regression Analysis (RA) models.

ANN models for predicting the axial compression strength of FRP-confined concrete circular columns were provided by Cascardi et al. [46]. A large database, including CFRP and GFRP FRP-confined concrete specimens, was analyzed in the study. Their ANN model with two dimensionless input factors was built, which includes quantitative measurements for the confinement stiffness of the FRP and the mechanical characteristics of unconfined concrete. The results demonstrated that the proposed model is adapted for the design of FRP-confined concrete and guarantees an improved accuracy. Elsanadedy et al. [48] have also provided a model for the compressive strength and ultimate strain of FRP-confined specimens with circular cross-sections using ANN and regression model, in which the input data includes five independent factors, which are the diameter of cylindrical specimen, the compressive strength of concrete, the thickness of FRP jacket, as well as the tensile strength and elastic modulus of FRP. The predictions of the ANN model were found to be more satisfactory than those of the regression-based models due to high correlation coefficients and insignificant estimated errors.

It is to be noted that the majority of ANN models have been performed using results of tests on FRP-confined circular concrete specimens [i.e., [49–60]]. Pham et al. [58] used ANN to predict both the compressive strength and corresponding strain of FRP confined noncircular concrete columns. A new predictive user-friendly approach is also provided to be used in practice. The test databases used to build the model are adopted from their previous studies [59,60]. The input ANN factors included the cross-sectional side length, the compressive strength of unconfined concrete and its corresponding strain, the tensile strength and elastic modulus of FRP, and the nominal thickness of FRP. The study generally yielded results with insignificant errors, approximately half of the errors from the existing RA models evaluated in their study.

Although many ANN and RA models are available for FRP-confined concrete, most of them are based on conventional FRP-confined unreinforced concrete columns. The goal of this paper is to provide a complete model for FRP confined concrete with and without internal steel reinforcement. The model consists of different approaches of ANN modeling and regression-based models. The database used in the analysis contains the experimental results of axial compression tests on a total of 226 circular and non-circular concrete specimens wrapped with PET and PEN FRPs. An easy-to-use approach is provided for predicting the strength and strain of FRP confined concrete columns. Furthermore,

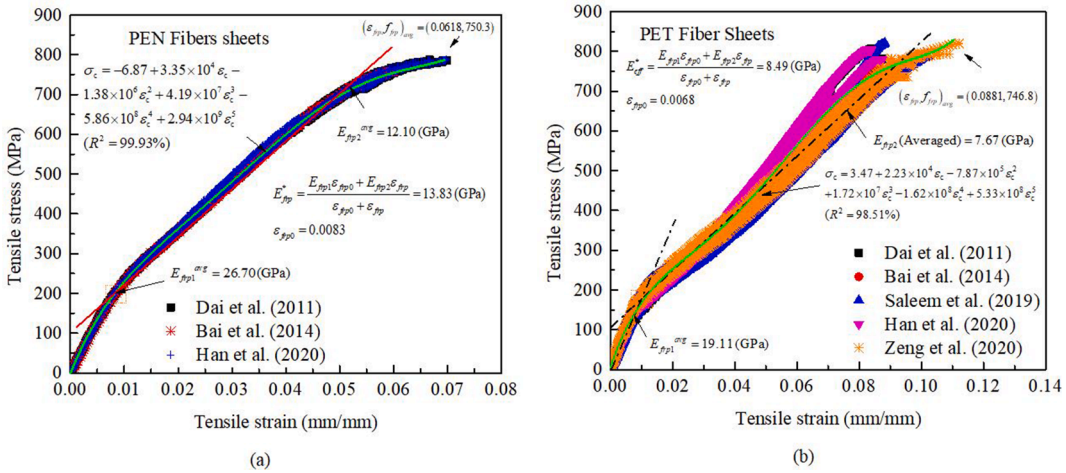

Fig. 6. Tensile stress–strain relationships of LRS FRP composites: (a) coupon tensile tests for PEN fiber sheets, (b) coupon tensile tests for PET fiber sheets.

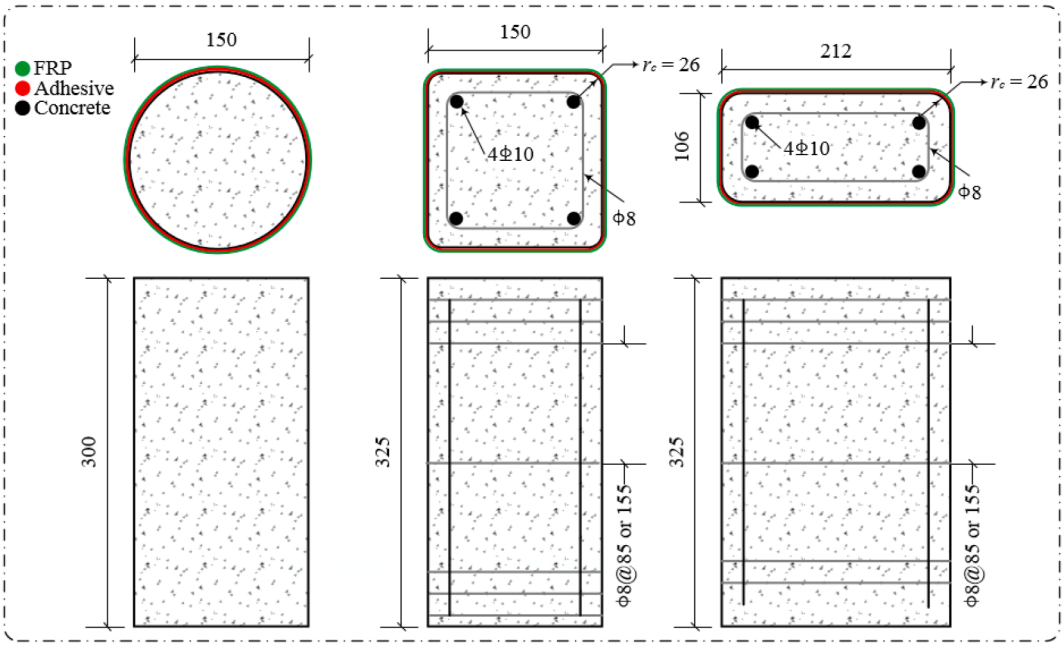

Fig. 7. Details of FRP-confined RC specimens (all dimensions in mm).

a new potential method to distinguish results that exhibit a post-peak strain-softening or strain-hardening behavior is introduced. The models are suitable for the design of FRP-confined RC columns and guarantee a safe design in regards to new test parameters.

2. Experimental databases

The database used to build the ANN and RA models was compiled through an extensive review of the available studies [29,30,32,33,35,36,40,42,61]. The number of specimens is 226 in total and they were tested under monotonic axial compression. The cross-sectional shape (i.e., circular, square, and rectangular), the corner radius, and the number of FRP layers were considered as the major variables in this paper. These concrete columns consisted of 61 square specimens, 21 rectangular specimens, and 144 circular specimens. All square specimens have a 150 × 150 mm cross-section, whereas the rectangular sections have a 106 × 212 mm cross-section. These specimens have a height of 300–325 mm. The circular ones are all standard concrete cylinders and have a diameter of 150–152 mm and a height of 300–305 mm. Among all the referred studies, only Saleem et al [33] have conducted tests on specimens with internal steel bars. The specimens have different corner radii (r_c) ranging from 0 to 75 mm (see Fig. 5). Among them, specimens with a 0 mm corner radius are square and rectangular as evidenced by their sharp corners, and those with a 75 mm corner radius are circular.

Other important variables which were also not considered in the existing literature are namely (1) varying amount of internal steel hoop reinforcement and (2) elastic modulus of LRS FRP through using PEN and PET FRPs, with E_f^*(defined as the effective tensile elastic modulus calculated by the proposed Eq. (1)), of 13.83 GPa and 8.49 GPa, respectively. Their mechanical properties including the coupon tensile stress–strain responses are all shown in Fig. 6. To consider the essential effects of steel reinforcement [74], the reinforced specimens had a longitudinal reinforcement ratio, ρ_s, of 1.43% (over the effectively confined concrete area, $[A_e = A_g\text{-}(4-\pi)r_c^2]$ (see Fig. 3) whereas the hoop reinforcement ratio, ρ_{ls}^*, varies from 0.32% to 0.78%. The yield strength of the internal longitudinal reinforcement (f_{yv}) and that of the

Table 1
Summary of tested circular specimens.

Strain enhancement ratio ($\varepsilon_{cu}/\varepsilon_{co}$)	13.80–31.18	12.51–31.90	24.18–57.38	26.23–56.03	10.58–55.35	11.94–41.80	19.25–34.41	15.08–46.52
Strength enhancement ratio (f_{cu}/f_{co})	1.28–2.68	1.33–3.01	1.83–4.91	1.61–3.79	1.21–3.92	1.99–4.13	0.78–2.39	1.27–4.07
Cylinder concrete strength, f_{co}: MPa	32.5–39.2	35.6–46.2	24.1	23.8	31.5–48.2	24.2	39.8–114.9	24.1–31.5
Height, *H*: mm	305	305	300	300	300	300	300	300
Diameter, *D*: mm	152	152	150	150	150	150	150	150
Fiber type	PEN & PET	PEN & PET	PET	PET	PEN & PET	PEN & PET	PET	PEN & PET
Specimens number, N	18	16	12	6	26	8	18	40
Researcher	Dai et al. [29]	Bai et al. [61]	Ispir et al. [40]	Saleem et al. [33]	Bai et al. [30]	Han et al. [36]	Zeng et al. [32]	Han Qiang et al. [42]
No.	1	2	3	4	5	6	7	8

Table 2
Summary of tested square and rectangular specimens.

Strain enhancement ratio ($\varepsilon_{cu}/\varepsilon_{c}$)	45.38–81.24	18.92–40.73	33.10–62.27
Strength enhancement ratio ($f_{cu}/f_{c}^{'}$)	0.63–2.42	0.80–3.96	0.90–3.27
Cylinder concrete strength, $f_{c}^{'}$: MPa	23.5–25.7	23.4–24.9	19.5–23.7
Corner radius, r_c : mm	0–26	0–60	26
Height, *H*: mm	300	300	325
Depth, *h*: mm	150–212	150	150–212
Width, *b*: mm	106–150	150	106–150
Fiber type	PET	PEN & PET	PET
Specimens number, N	18	40	24
Researcher	Saleem et al. [33]	Han et al. [36]	Saleem et al. [35]
No.	1	2	3

hoop steel bars (f_{yh}) are 508 MPa and 375 MPa, respectively. The cross-section and steel reinforcement details of the specimens are shown in Fig. 7.

$$E_{frp}^{*} = \frac{E_{frp1}\varepsilon_{frp0} + E_{frp2}\varepsilon_{frp}}{\varepsilon_{frp0} + \varepsilon_{frp}} \quad (1)$$

where for LRS FRPs which exhibited a tri-linear tensile stress–strain response as described in Fig. 6,E_{frp1} is the modulus of the first linear portion of the stress–strain relationship, and E_{frp2} is the modulus of the second linear portion; $\varepsilon_{frp0}$is the strain where the elastic modulus of the FRP sheets changes; $\varepsilon_{frp}$is the ultimate tensile strain at FRP failure.

Generally, all specimens were fully FRP confined concrete, and among all tests, the number of specimens with a full stress–strain response including the dilation behavior is 200 from all studies except [35]. In the test database, the tested $v_{s,max} = \varepsilon_{lcu}/\varepsilon_{cu}$, defined as the ratio between the lateral to axial strain at failure, is in the range of 0.37–1.79 with mean and SR of 0.95 and 0.29, respectively; the strength enhancement ratio, defined as the ratio of the ultimate strength of confined column to the concrete compressive strength of unwrapped standard cylinder, is in the range of 0.64–4.49 with mean and SR of 2.09 and 0.91, respectively; $f_{c}^{'}$is in the range of 19.5–114.9 MPa with mean and standard deviation (SR) of 25.6 MPa and 17.24 MPa, respectively; $n_{frp} \times t_{frp}$ (total thickness of FRP jacket) is in the range of 0.84–3.79 mm with mean and SR of 1.68 mm and 0.78 mm, respectively; the actual confinement ratio, defined as the ratio of the nominal confining pressure, $f_{lf,o}$, [calculated using Eq. (2)] to the$f_{c}^{'}$value, varied from 5.5 to 42.0 MPa with mean and SR of 16.6 MPa and 8.6 MPa, respectively; the tested confinement ratio, defined as the ratio of the confining pressure estimated using the averaged value of hoop rupture strain from tests, $f_{lf,a}$, [calculated using Eq. (3)] to the $f_{c}^{'}$value, varied from 3.0 to 34.4 MPa with mean and SR of 11.3 MPa and 7.3 MPa, respectively; the

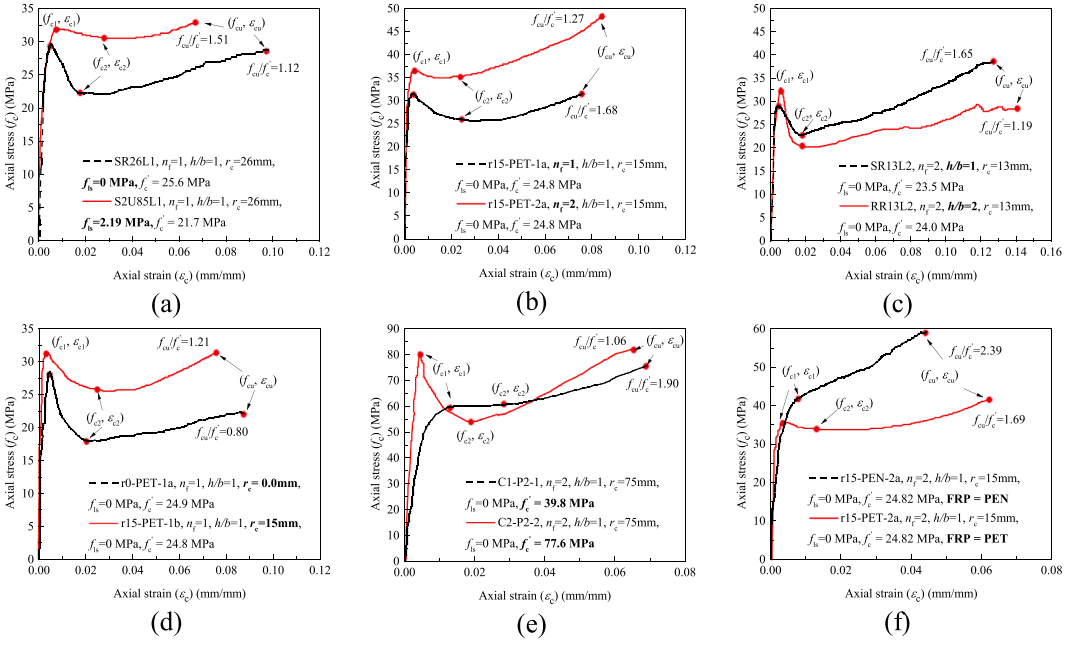

Fig. 8. Stress–strain relationships of selected FRP-confined concrete considering the effects of column parameters.

Table 3
Evaluation of Lim and Ozbakkaloglu [15]'s model.

No.	Code	Section shape	Response Type	$f_c^{'}$(MPa)	K_l	K_{lo}	Model Prediction	Marked
1	r40-PET-2-a	Square	Strain Hardening	23.4	283.9	181.0	Strain Hardening	✓
2	r60-PET-1-a	Square	Strain Hardening	24.6	141.9	197.0	Strain softening	×
3	r60-PET-2-a	Square	Strain Hardening	24.6	283.9	197.0	Strain Hardening	✓
4	r15-PEN-2-a	Square	Strain Hardening	24.8	647.6	200.2	Strain Hardening	✓
5	r25-PEN-2-a	Square	Strain Hardening	24.6	647.6	197.8	Strain Hardening	✓
6	r40-PEN-1-a	Square	Strain Hardening	23.4	323.8	181.0	Strain Hardening	✓
7	r40-PEN-2-a	Square	Strain Hardening	23.4	647.6	181.0	Strain Hardening	✓
8	r60-PEN-1-a	Square	Strain Hardening	24.6	323.8	197.0	Strain Hardening	✓
9	r60-PEN-2-a	Square	Strain Hardening	24.6	647.6	197.0	Strain Hardening	✓
10	SR26L3	Square	Flat Response	25.6	468.6	210.9	Strain Hardening	×
11	r25-PET-2-a	Square	Flat Response	24.6	283.9	197.8	Strain Hardening	×
12	r40-PET-1-a	Square	Flat Response	23.4	141.9	181.0	Strain softening	×
13	r15-PEN-1-a	Square	Flat Response	24.8	323.8	200.2	Strain Hardening	×
14	SR0L1	Square	Strain Softening	25.6	156.2	210.9	Strain softening	✓
15	r0-PEN-1-a	Square	Strain Softening	24.9	323.8	201.2	Strain Hardening	×
16	r0-PEN-2-a	Square	Strain Softening	24.9	647.6	201.2	Strain Hardening	×
17	r0-PET-1-a	Square	Strain Softening	24.9	141.9	201.2	Strain softening	✓
18	r0-PET-2-a	Square	Strain Softening	24.9	283.9	201.2	Strain Hardening	×
19	SR0L2	Square	Strain Softening	23.5	312.4	182.3	Strain Hardening	×
20	SR0L3	Square	Strain Softening	25.6	468.6	210.9	Strain Hardening	×
21	SR13L1	Square	Strain Softening	23.5	156.2	182.3	Strain softening	✓
22	SR13L2	Square	Strain Softening	23.5	312.4	182.3	Strain Hardening	×
23	SR13L3	Square	Strain Softening	23.5	468.6	182.3	Strain Hardening	×
24	SR26L1	Square	Strain Softening	25.6	156.2	210.9	Strain softening	✓
25	SR26L2	Square	Strain Softening	23.5	312.4	182.3	Strain Hardening	×
26	r25-PET-1-a	Square	Strain Softening	24.6	141.9	197.8	Strain softening	✓
27	r15-PET-1-a	Square	Strain Softening	24.8	141.9	200.2	Strain softening	✓
28	r15-PET-2-a	Square	Strain Softening	24.8	283.9	200.2	Strain Hardening	×
29	RR0L1	Rectangular	Strain Softening	25.7	139.8	211.9	Strain softening	✓
30	RR0L2	Rectangular	Strain Softening	25.7	279.6	211.9	Strain Hardening	×
31	RR0L3	Rectangular	Strain Softening	25.7	419.4	211.9	Strain Hardening	×
32	RR13L1	Rectangular	Strain Softening	24.0	139.8	189.4	Strain softening	✓
33	RR13L2	Rectangular	Strain Softening	24.0	279.6	189.4	Strain Hardening	×
34	RR13L3	Rectangular	Strain Softening	24.0	419.4	189.4	Strain Hardening	×
35	RR26L1	Rectangular	Strain Softening	24.0	139.8	189.4	Strain softening	✓
36	RR26L2	Rectangular	Strain Softening	24.0	279.6	189.4	Strain Hardening	×
37	RR26L3	Rectangular	Strain Softening	24.0	419.4	189.4	Strain Hardening	×
38	PET600-1–1	Circular	Flat Response	32.5	198.1	312.3	Strain softening	×
39	R0-PET-1-a	Circular	Flat Response	31.5	200.7	296.6	Strain softening	×
40	R33-PET-1-a	Circular	Flat Response	28.6	200.7	252.9	Strain softening	×
41	C1L1	Circular	Flat Response	23.8	220.9	186.7	Strain Hardening	×
42	C1–P3-1	Circular	Strain Hardening	39.8	635.8	436.3	Strain Hardening	✓
43	1P-M−a	Circular	Strain Hardening	24.1	313.0	190.7	Strain Hardening	✓
44	2P-M−a	Circular	Strain Hardening	24.1	626.0	190.7	Strain Hardening	✓
45	3P-M−a	Circular	Strain Hardening	24.1	938.9	190.7	Strain Hardening	✓
46	1P-C-a	Circular	Strain Hardening	24.1	313.0	190.7	Strain Hardening	✓
47	2P-C-a	Circular	Strain Hardening	24.1	626.0	190.7	Strain Hardening	✓
48	3P-C-a	Circular	Strain Hardening	24.1	938.9	190.7	Strain Hardening	✓
49	S1	Circular	Strain Hardening	33.2	301.2	323.5	Strain softening	×
50	S11	Circular	Strain Hardening	48.2	301.2	598.4	Strain softening	×
51	S17	Circular	Strain Hardening	31.5	200.7	296.6	Strain softening	×
52	PET600-2–1	Circular	Strain Hardening	32.5	396.2	312.3	Strain Hardening	✓
53	PET600-3–1	Circular	Strain Hardening	32.5	594.2	312.3	Strain Hardening	✓
54	R0-PET-2-a	Circular	Strain Hardening	31.5	401.4	296.6	Strain Hardening	✓
55	R33-PET-2-a	Circular	Strain Hardening	28.6	401.4	252.9	Strain Hardening	✓
56	R67-PET-1-a	Circular	Strain Hardening	25.6	200.7	210.7	Strain softening	×
57	R67-PET-2-a	Circular	Strain Hardening	25.6	401.4	210.7	Strain Hardening	✓
58	R100-PET-1-a	Circular	Strain Hardening	24.1	200.7	190.7	Strain Hardening	✓
59	R100-PET-2-a	Circular	Strain Hardening	24.1	401.4	190.7	Strain Hardening	✓
60	C-P1-1	Circular	Strain Hardening	24.8	196.0	199.9	Strain softening	×
61	C-P2-1	Circular	Strain Hardening	24.8	392.0	199.9	Strain Hardening	✓
62	C-P3-1	Circular	Strain Hardening	24.8	588.0	199.9	Strain Hardening	✓
63	r75-PEN-1-a	Circular	Strain Hardening	24.2	457.9	191.3	Strain Hardening	✓
64	r75-PEN-2-a	Circular	Strain Hardening	24.2	915.8	191.3	Strain Hardening	✓
65	r75-PET-1-a	Circular	Strain Hardening	24.2	200.7	191.3	Strain Hardening	✓
66	r75-PET-2-a	Circular	Strain Hardening	24.2	401.4	191.3	Strain Hardening	✓
67	PEN-b1-1-A	Circular	Strain Hardening	35.6	451.9	363.0	Strain Hardening	✓
68	PEN-b1-2-A	Circular	Strain Hardening	35.6	903.8	363.0	Strain Hardening	✓
69	PET-b1-1-A	Circular	Strain Hardening	35.6	198.1	363.0	Strain softening	×
70	PET-b1-2-A	Circular	Strain Hardening	35.6	396.2	363.0	Strain Hardening	✓
71	PEN-b2-1-A	Circular	Strain Hardening	46.2	451.9	558.0	Strain softening	×
72	PEN-b2-2-A	Circular	Strain Hardening	46.2	903.8	558.0	Strain Hardening	✓
73	PET-b2-2-A	Circular	Strain Hardening	46.2	396.2	558.0	Strain softening	×

(*continued on next page*)

Table 3 (*continued*)

74	PET-b2-3-A	Circular	Strain Hardening	46.2	594.2	558.0	Strain Hardening	✓
75	C1L2	Circular	Strain Hardening	23.8	441.8	186.7	Strain Hardening	✓
76	C1L3	Circular	Strain Hardening	23.8	662.7	186.7	Strain Hardening	✓
77	S3	Circular	Strain Hardening	33.2	602.4	323.5	Strain Hardening	✓
78	S5	Circular	Strain Hardening	33.2	903.6	323.5	Strain Hardening	✓
79	S7	Circular	Strain Hardening	33.2	457.9	323.5	Strain Hardening	✓
80	S9	Circular	Strain Hardening	33.2	915.8	323.5	Strain Hardening	✓
81	S13	Circular	Strain Hardening	48.2	602.4	598.4	Strain Hardening	✓
82	S15	Circular	Strain Hardening	48.2	903.6	598.4	Strain Hardening	✓
83	S19	Circular	Strain Hardening	31.5	401.4	296.6	Strain Hardening	✓
84	S21	Circular	Strain Hardening	31.5	602.2	296.6	Strain Hardening	✓
85	S23	Circular	Strain Hardening	31.5	457.9	296.6	Strain Hardening	✓
86	S25	Circular	Strain Hardening	31.5	915.8	296.6	Strain Hardening	✓
87	PEN-1–1	Circular	Strain Hardening	39.2	301.3	425.5	Strain softening	×
88	PEN-2–1	Circular	Strain Hardening	39.2	602.5	425.5	Strain Hardening	✓
89	PEN-3–1	Circular	Strain Hardening	39.2	903.8	425.5	Strain Hardening	✓
90	R0-PET-3-a	Circular	Strain Hardening	31.5	602.2	296.6	Strain Hardening	✓
91	R33-PET-3-a	Circular	Strain Hardening	28.6	602.2	252.9	Strain Hardening	✓
92	R67-PET-3-a	Circular	Strain Hardening	25.6	602.2	210.7	Strain Hardening	✓
93	R100-PET-3-a	Circular	Strain Hardening	24.1	602.2	190.7	Strain Hardening	✓
94	R0-PEN-1-a	Circular	Strain Hardening	31.5	457.9	296.6	Strain Hardening	✓
95	R0-PEN-2-a	Circular	Strain Hardening	31.5	915.8	296.6	Strain Hardening	✓
96	R33-PEN-1-a	Circular	Strain Hardening	28.6	457.9	252.9	Strain Hardening	✓
97	R33-PEN-2-a	Circular	Strain Hardening	28.6	915.8	252.9	Strain Hardening	✓
98	R67-PEN-1-a	Circular	Strain Hardening	25.6	457.9	210.7	Strain Hardening	✓
99	R67-PEN-2-a	Circular	Strain Hardening	25.6	915.8	210.7	Strain Hardening	✓
100	R100-PEN-1-a	Circular	Strain Hardening	24.1	457.9	190.7	Strain Hardening	✓
101	R100-PEN-2-a	Circular	Strain Hardening	24.1	915.8	190.7	Strain Hardening	✓
102	C1–P2-1	Circular	Strain Hardening	39.8	423.9	436.3	Strain softening	×
103	C1–P1-1	Circular	Strain Softening	39.8	211.9	436.3	Strain softening	✓
104	C2–P2-1	Circular	Strain Softening	77.6	423.9	1313.0	Strain softening	✓
105	C2–P3-1	Circular	Strain Softening	77.6	635.8	1313.0	Strain softening	✓
106	C2–P4-1	Circular	Strain Softening	77.6	847.7	1313.0	Strain softening	✓
107	C3–P2-1	Circular	Strain Softening	114.9	423.9	2509.2	Strain softening	✓
108	C3–P3-1	Circular	Strain Softening	114.9	635.8	2509.2	Strain softening	✓
109	C3–P4-1	Circular	Strain Softening	114.9	847.7	2509.2	Strain softening	✓

volumetric ratio of hoop steel reinforcement ρ_{ls}^{*} is in the range of 0.32–0.79 % with mean and SR of 0.51 % and 0.18 %, respectively. General summaries for the specimens are provided in Tables 1 and 2, respectively for circular and noncircular specimens. Other details such as test design, instrumentation, and testing can be found in the cited studies.

$$f_{lf,o} = K_{lf}\varepsilon_{frp} = \frac{2n_{frp}t_{frp}E_{frp}^{*}}{d_e}\varepsilon_{frp} = 0.5\rho_{frp}E_{frp}^{*}\varepsilon_{frp} \quad (2)$$

$$f_{lf,a} = K_{lf}\varepsilon_{h,rup} = \frac{2n_{frp}t_{frp}E_{frp}^{*}}{d_e}\varepsilon_{h,rup} = 0.5\rho_{frp}E_{frp}^{*}\varepsilon_{h,rup} \quad (3)$$

where n_{frp} and t_{frp} are respectively the number of FRP layers and the nominal thickness of the fiber sheets; E_{frp}^{*} is the effective tensile elastic modulus as given by Eq. (1); ε_{frp} is the ultimate FRP strain from coupon tensile tests and $\varepsilon_{h,rup}$ is the FRP hoop rupture strain; ρ_{frp} is the volumetric ratio of transverse FRP wraps ($\rho_{frp} = 4n_{frp}t_{frp}/d_e$); d_e is the equivalent diameter of a rectangular section; $d_e = \sqrt{b^2 + h^2}$ where b and h are the width and depth of a rectangular cross-section, respectively.

3. Shape of Stress-Strain response recognition

3.1. General

Fig. 8 shows comparisons between selected stress–strain relationships from Zeng et al. [32], Saleem et al. [33,35], and Han et al. [42]. As illustrated, the axial stress–strain responses consist of an ascending portion that is followed by one continuous branch or two distinct branches. In general, the stress–strain curve may exhibit a full strain hardening behavior (i.e., r15-PEN-2a in Fig. 8f), or it may consist of a second branch as an initial strain softening region (i.e., C2-P2-2 in Fig. 8e) which may be subsequently recovered or may not be recovered. The axial stress and strain corresponding to the initial peak (f_{c1},ε_{c1}), second transition point (f_{c2},ε_{c2}), and ultimate condition (f_{cu},ε_{cu}) are marked in Fig. 8.

The model provided in this paper considers three major classes of stress–strain responses, namely a stress–strain response that consists of an ascending first portion followed by a continuous flat, descending, or a slightly ascending branch (with or without strain softening) (i.e., Class (1), $f_{cu} \leq f_{c1}$), a partially-recovered stress–strain response with initial strain-softening that is followed by an overall ascending third branch (i.e., Class (2), $f_{cu} > f_{c1}$), and a fully-recovered stress–strain response. In this paper, fully-recovered type is any response without initial strain-softening that is followed by one continuous ascending branch or a flat second branch that is finally followed by an ascending branch (i.e., Class (3), $f_{cu} > f_{c1}$).

4. 3.2.Regression-Based-Model

The comparisons provided in Table 3 between the predictions of the Ref. [15]'s model and the actual results of 109 specimens only due to the replication of tests, in general, show that this model that is developed for traditional FRP confined circular specimens is not able to distinguish between the different stress–strain curves of LRS FRP-confined concrete specimens. More clearly, many of the stress–strain responses, in particular for rectangular specimens, are not well quantified, while many of the responses of circular specimens are in a good way distinguished. It is therefore intended in this paper to expand the application of the model based on the compiled LRS FRP-confined tests. New expressions for rectangular specimens are also provided as follows:

For FRP-confined concrete to exhibit a fully-recovered stress–strain response with no initial strain softening, the confinement stiffness of the FRP jacket [$K_{lf} = 0.5\rho_{frp}E_{frp}^{*}$; Eq. (2)] should exceed a certain

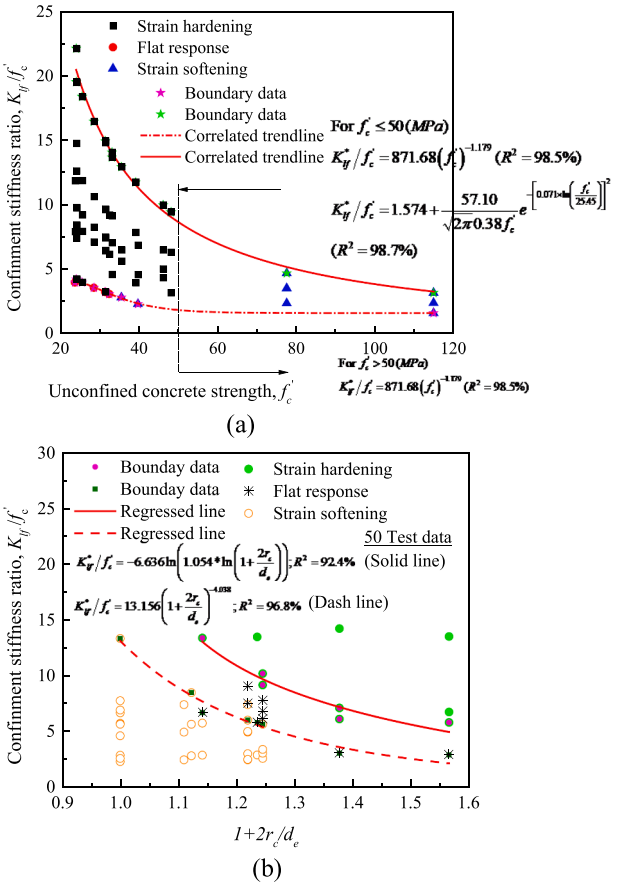

Fig. 9. Threshold confinement stiffness for specimens distinguished based on their response type, namely post-peak strain hardening behavior; strain-softening behavior; flat-ascending behavior: (a) For circular specimens; (b) For rectangular specimens.

confinement threshold level (K_{lf}^*). Because of the varying confinement effectiveness due to the variations in test parameters, the accurate estimation of the threshold level of FRP confinement is of significant importance for a safe design of FRP-confined concrete. The rectangular specimens considered in this paper had smaller values of unconfined confined strength, which is in the range of 19.5–25.7 MPa, compared with a greater range of 23.8–114.9 MPa for circular specimens. Therefore, in Fig. 9(a and b), the relationships are drawn based on the available test parameters. The regressed relationships are correlated based on the general boundaries of the different stress–strain response types.

Fig. 9(a) shows the relationship between comparable confinement stiffness and the variation of compressive strengths of unconfined concrete. The FRP confinement stiffness varies concerning the change in the unconfined concrete strength. For circular specimens, the number of FRP confinement layers, the unconfined concrete compressive strength, and the type of LRS FRP confining material were the major variables in the present analysis. Based on this understanding and the compiled test results, the variation of the normalized confinement stiffness and f_c' was carefully examined for all circular specimens. This resulted in the development of Eqs. (4–6) to accurately determine K_{lf}^* based on the relationships illustrated in Fig. 9(a), in which the proposed model (i.e., Eq. (4)) is composed of two different forms to represent the difference in results for low strength concrete mostly exhibit strain hardening behavior and unconfined concrete strength of larger than 50 MPa with a strain-softening behavior.

$$\begin{cases} K_{lf}/f_c' > K_{lf}^*/f_c'; K_{lf}^*/f_c' = 871.68(f_c')^{-1.179}; f_c' > 50 \text{ (MPa)} \\ K_{lf}/f_c' > K_{lf}^*/f_c'; K_{lf}^*/f_c' = 1.574 + \dfrac{57.10}{\sqrt{2\pi}0.38f_c'} e^{-\left[0.071\times ln\left(\frac{f_c'}{25.45}\right)\right]^2}; 23.8(\text{MPa}) \\ < f_c' < 50(\text{MPa}) \end{cases}$$

(For-strain hardening)(Eq. 4)

$$K_{lf}/f_c' = K_{lf}^*/f_c'; K_{lf}^*/f_c' = 1.574 + \frac{57.10}{\sqrt{2\pi}0.38f_c'} e^{-\left[0.071\times ln\left(\frac{f_c'}{25.45}\right)\right]^2}; f_c' \leqslant 50 \quad (\text{MPa})$$

(For flat-ascending response) (Eq. 5)

$$\begin{cases} K_{lf}/f_c' \leqslant K_{lf}^*/f_c'; K_{lf}^*/f_c' = 871.68(f_c')^{-1.179}; f_c' > 50 \text{ (MPa)} \\ K_{lf}/f_c' \leqslant K_{lf}^*/f_c'; K_{lf}^*/f_c' = 1.574 + \dfrac{57.10}{\sqrt{2\pi}0.38f_c'} e^{-\left[0.071\times ln\left(\frac{f_c'}{25.45}\right)\right]^2}; 23.8(\text{MPa}) \\ < f_c' < 50(\text{MPa}) \end{cases}$$

(For strain softening)(Eq. 6)

As already mentioned before, the rectangular specimens had a limited range of unconfined confined strength compared with circular ones. Due to the limited tests and variables considered for the rectangular specimens, the ratio of the corner radius to the diameter of the rectangular section is chosen as the dominant influencing parameter. As shown in Fig. 9(b), the FRP confinement stiffness decreases with the increase of the corner radius ratio. That is because the uniformity of the confining pressure distribution increases as the $2r_c/d_e$ increases, and consequently the confinement stiffness threshold that is required for a strain hardening decreases. For rectangular specimens, Eqs. (7–9) are proposed as

$$K_{lf}/f_c' \geqslant K_{lf}^*/f_c'; K_{lf}^*/f_c' = -6.636ln\left(1.054*ln\left(1+\frac{2r_c}{d_e}\right)\right)$$

(For-strain hardening) (Eq. 7)

$$13.156\left(1+\frac{2r_c}{d_e}\right)^{-4.038} \leqslant K^*_{lf}\Big/f_c' < -6.636ln\left(1.054*ln\left(1+\frac{2r_c}{d_e}\right)\right)$$

(For flat-ascending response) (Eq. 8)

$$K_{lf}/f_c' < K_{lf}^*/f_c'; K_{lf}^*/f_c' = 13.156\left(1+\frac{2r_c}{d_e}\right)^{-4.038}$$

(For strain softening) (Eq. 9)

4.1. ANN model

The ANN application is widely used for classification, pattern recognition, and prediction or modeling. In particular, the use of ANN for predicting the compressive strength and strain of confined concrete has been studied [i.e., [49,61]. However, the use of ANN for FRP-confined concrete as a classification problem to predict whether the concrete will have a strain hardening or softening has not yet been explored. In the aim of this, the ANN classification model for all specimens was firstly structured and then trained using *R Language Programming*.

The database was randomly divided into training (70%) and test (30%) one at a time. Based on discussions and suggestions provided by different researchers [62-65,67], to design a stable network and guarantee a generalization of the network, one hidden layer was selected and the number of hidden neurons was determined by training several networks across a wide range of parameters with the help of the caret

Table 4
Details of the five neural network models.

Model	Test accuracy	Train accuracy	(test/train) ratio	Structure	decay/learning rate
neuralnet	0.88	0.99	88.89	N6-4–3	1.00E-02
multinom	0.91	0.97	93.81	N6-0–3	1.00E-03
mxnet	0.87	0.97	89.69	N6-4–3	1.00E-01
nnet	0.90	1.00	90.00	N6-6–3	1.10E-02
mlp	0.85	1.00	85.00	N6-4–3	2.00E-01

package in *R Language Programming*. Furthermore, five different ANN models namely neuralnet, multinom, nnet, mlp, and mxnet were considered.

The ANN models consist of six input nodes, three output nodes, and the number of nodes in the hidden layer varies from 0 to 9, which is assumed to be the sum of the numbers of input and output nodes. The input variables are arranged as *h*or $DC_r = 2r_c/bf_c^{'}\varepsilon_{fu}(\varepsilon_{frp})FRPs = n_{frp}t_{frp}E_{frp}^{*}$and*HSS*referred to as$f_{ls}$. The three output nodes correspond to Classes 1, 2, and 3 of stress–strain responses, and the numbers of a dataset corresponding to the three classes are 27, 21, and 112, respectively. ANN model with six input and three output nodes will be referred to as N6-0–3 (without a hidden layer). Regardless of the number of neurons in the hidden layer, the major objective of this analysis is to propose the simplest and most accurate ANN model which can reasonably simulate the behavior of FRP-confined reinforced concrete.

Table 4 shows the comparison of the accurate measurement of the models, both for training and test data. All models, except the mxnet

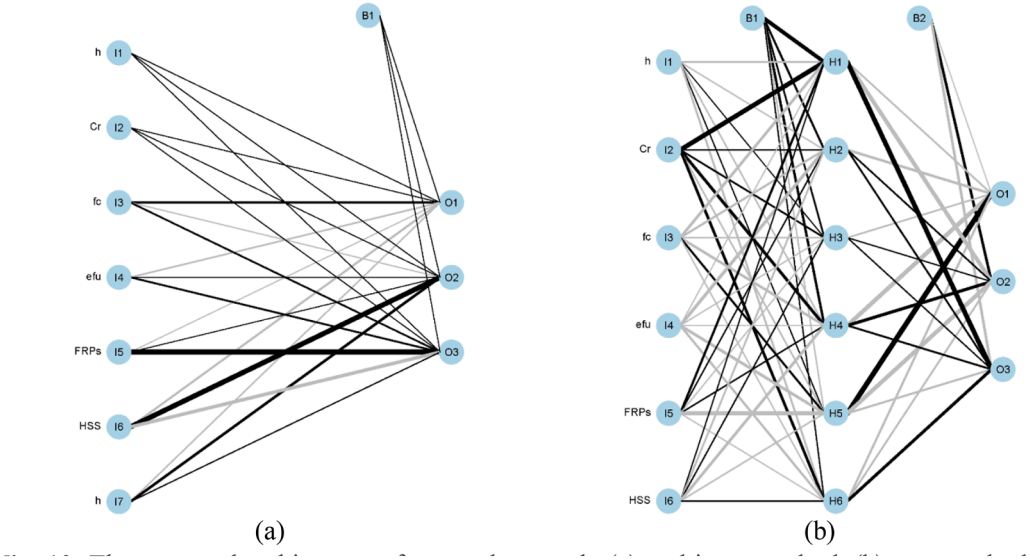

Fig. 10. The proposed architecture of a neural network: (a) multinom method; (b) nnet method.

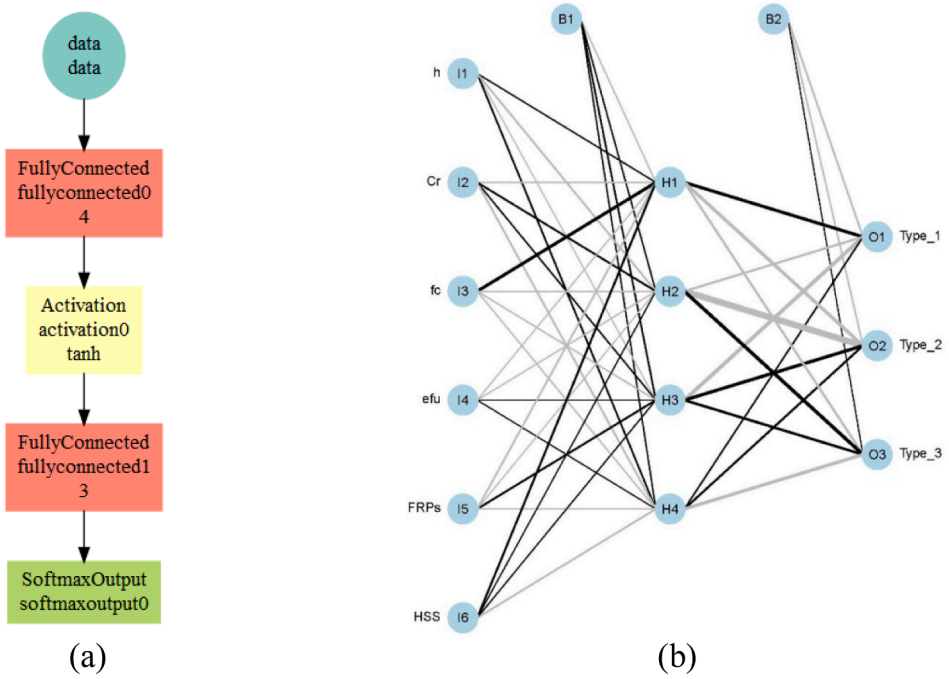

Fig. 11. The proposed architecture of a neural network: (a) mxnet method; (b) neuralnet method.

Table 5
Values for scaling the inputs' data.

Input/Output		Maximum	Minimum	Mean	Standard Deviation	No. of data
h	mm	212.0	150.0	158.36	20.92	226
$2r_c/b$	mm/mm	1.00	0.00	0.673	0.366	226
$f_c^{'}$	MPa	114.90	19.50	29.81	14.87	226
ε_{fu}	mm/mm	0.100	0.058	0.081	0.014	226
$E_f^* n_f t_f$	N.mm	35305.19	6798.07	18343.86	9191.73	226
$\rho_{ls}^* f_{yh}$	MPa	2.95	0.00	0.30	0.76	226
$f_{cc}^{'}/f_c^{'}$	–	1.70	1.02	1.25	0.15	70
ε_{cc}	mm/mm	0.0127	0.0032	0.0053	0.0022	70
$f_{cu}^{'}/f_c^{'}$	–	4.49	0.64	2.07	0.86	226
ε_{cu}	mm/mm	0.1762	0.0252	0.0709	0.0273	226

model, revealed a very small learning rate compared with the value of 0.01 used in Ref. [58]. It can be also seen that the N6-0–3 model using the multinom has the highest accuracy for both training and test data. However, it should be noted that this model does not have a hidden layer and most importantly the results obtained from the software have not well considered the first type of stress–strain response decoded as Class 1. This means the relative importance of the input variables to the first output is insignificant as it can be understood by the insignificant width of the black-colored connection in Fig. 10a. On the other hand, the first and third types of responses (Class 1 and 3) are shown to be more dominant in the nnet model (see Fig. 10b). The relative importance values of input parametersC_r, $f_c^{'}$, ε_{frp}, *FRPs, HSS, and h*or *D*obtained by the nnet method are respectively 100.00, 61.50, 42.88, 31.67, 25.64, and 0.00, whereas those from the multinom model are respectively 100.00, 60.86, 49.29, 21.26, 21.26, 7.98, and 0.00. The two most significant input parameters are $C_r = 2r_c/b$(100%), $f_c^{'}$(61.50% by the nnet model and 60.86% by the multinom model). Because of the importance of these two variables, a significant number of models are introduced for the behavior of concrete with varying FRP confinement stiffness ratios [i.e., [9–21].

However, the models that often reveal a superior accuracy particularly in the training data may not be reasonable. The accuracy levels of mxnet (Fig. 11a) and neuralnet (Fig. 11b) models are very close and these models have the same ANN structures (i.e., N6-4–3) compared with the N6-6–3 provided by the nnet method. ANN architecture with the minimum number of hidden nodes would be reasonable [46]. One of the major differences between these two networks is the use of different activation functions between the ANN layers. In mxnet model, the tanh activation function was utilized between the input and the middle hidden layer, whereas a softmax function was between the output data of the hidden layer and the final output layer. In neuralnet model, the logistic activation functions were utilized between all layers, and as a result, this is more convenient to be integrated or differentiated to generate an easy-to-use model in engineering design.

It is to be noted that all the inputs' data are first normalized using the mean ($\overline{x_j}$) and standard deviation (σ_j) of each input variable (Table 5). The relationship between the actual inputs and the actual normalized inputs is presented in Eq. (10). The final results of the weights and biases of the N 6–4-3 neuralnet model are shown in Eqs. (11–14).

$$x_j = \frac{x_{ij} - \overline{x_j}}{\sigma_j} \tag{10}$$

$$w_1 = \begin{bmatrix} 1.750 & -5.33 & 15.92 & -0.90 & -5.26 & 7.84 \\ -5.90 & 5.72 & -3.60 & -1.71 & -0.42 & 0.64 \\ -0.49 & 2.79 & -2.69 & 0.97 & 6.67 & 1.01 \\ 4.99 & -5.96 & -2.02 & 0.22 & -5.63 & -5.86 \end{bmatrix} \tag{11}$$

$$w_2 = \begin{bmatrix} 16.57 & -8.87 & -20.82 & 3.55 \\ -16.88 & -42.52 & 17.33 & 7.71 \\ -8.95 & 18.52 & 11.91 & -17.12 \end{bmatrix} \tag{12}$$

$$b_1 = \begin{bmatrix} -2.15 \\ 2.52 \\ 5.01 \\ 2.42 \end{bmatrix} \tag{13}$$

$$b_2 = \begin{bmatrix} -5.75 \\ -3.66 \\ 0.48 \end{bmatrix} \tag{14}$$

where w_1 is the weight matrix between the input layer and the hidden layer;w_2 is the weight matrix between the hidden layer and the output layer, b_1 and $b_2$are the bias matrices of the hidden and output layers (see Fig. 11b).

The practically used ANN model with four hidden neurons, six input variables, and three output variables is described. Now, the weights provided in Eq. (11) are first multiplied with a transposed input matrix (x=$[x_1, x_2, x_3, x_4, x_5, x_6]^T$) and then adding the values of (b_1[Eq. (13)]). The total sum ($w_1 x + b_1$) is then substituted into the sigmoid activation function as in Eq. (15) and the predictions from the hidden layer are represented by Eq. (16) of values with the same hidden nodes' number.

$$v_i = \frac{1}{1 + e^{-[(w_{h1}x + w_{h2}x + w_{h3}x + w_{h4}x) + b1]}} \tag{15}$$

$$v = \begin{bmatrix} v_1 \\ v_2 \\ v_3 \\ v_4 \end{bmatrix} \tag{16}$$

where w_{h1} w_{h2} w_{h3} and $w_{h4}$are the weights of the four hidden nodes (Eq. (11)).

Now, taking the results of Eq. (16) as a new input data for the output layer and repeating the same procedure in Eq. (17) will give results as in Eq. (18) of values with the same number of output nodes. The type of stress–strain response can now be recognized as Class 1 if the values (i.e., y_1,y_2,y_3) are 1,0,0, and if these values are 0,1,0, then it is Class 2, otherwise, it is Class 3. It is revealed that the number of specimens in Table 6 that failed to be recognized by the proposed model is 6, showing better performance than the model in Ref. [15] (Table 3).

$$y_i = \frac{1}{1 + e^{-[(w_{o1}v + w_{o2}v + w_{o3}v) + b2]}} \tag{17}$$

$$y = [y_1 \quad y_2 \quad y_3] \tag{18}$$

where w_{o1}, w_{o2}, and $w_{o3}$are the weights of the three output nodes (Eq. (12)).

Table 6
Evaluation of ANN model [Eqs.(10–18)].

No	Author	Scaled Inputs (Eq. (10)						Type	Layer 1 (Eqs. 15–16)				Layer 2 (Eqs. 17–18)			Model	Marked
		h (mm)	$2r_c/b$ (mm/mm)	f_c' (MPa)	ε_{fu} (mm/mm)	$E_f^* n_f t_f$	$\rho_{is}^* f_{yh}$		v1	v2	v3	v4	y1	y2	y3		
1	Han et al.	−0.400	−1.841	−0.330	−1.669	−0.075	−0.394	1	0.63	0.14	0.17	1.00	1	0	0	1	Succeed
2	[36]	−0.400	−1.841	−0.330	−1.669	−0.075	−0.394	1	0.63	0.14	0.17	1.00	1	0	0	1	Succeed
3		−0.400	−1.841	−0.330	−1.669	1.845	−0.394	2	0.00	0.07	1.00	0.97	0	1	0	2	Succeed
4		−0.400	−1.841	−0.330	−1.669	1.845	−0.394	2	0.00	0.07	1.00	0.97	0	1	0	2	Succeed
5		−0.400	−1.841	−0.330	0.129	−1.170	−0.394	1	0.99	0.01	0.00	1.00	1	0	0	1	Succeed
6		−0.400	−1.841	−0.330	0.129	−1.170	−0.394	1	0.99	0.01	0.00	1.00	1	0	0	1	Succeed
7		−0.400	−1.841	−0.330	0.129	−0.344	−0.394	1	0.58	0.01	0.17	1.00	1	0	0	1	Succeed
8		−0.400	−1.841	−0.330	0.129	−0.344	−0.394	1	0.58	0.01	0.17	1.00	1	0	0	1	Succeed
9		−0.400	−1.294	−0.336	−1.669	−0.075	−0.394	3	0.08	0.79	0.50	1.00	0	0	1	3	Succeed
10		−0.400	−1.294	−0.336	−1.669	−0.075	−0.394	3	0.08	0.79	0.50	1.00	0	0	1	3	Succeed
11		−0.400	−1.294	−0.336	−1.669	1.845	−0.394	3	0.00	0.63	1.00	0.59	0	0	1	3	Succeed
12		−0.400	−1.294	−0.336	−1.669	1.845	−0.394	3	0.00	0.63	1.00	0.59	0	0	1	3	Succeed
13		−0.400	−1.294	−0.336	0.129	−1.170	−0.394	1	0.84	0.21	0.00	1.00	1	0	0	1	Succeed
14		−0.400	−1.294	−0.336	0.129	−1.170	−0.394	1	0.84	0.21	0.00	1.00	1	0	0	1	Succeed
15		−0.400	−1.294	−0.336	0.129	−0.344	−0.394	2	0.06	0.16	0.48	1.00	0	1	0	2	Succeed
16		−0.400	−1.294	−0.336	0.129	−0.344	−0.394	2	0.06	0.16	0.48	1.00	0	1	0	2	Succeed
17		−0.400	−0.929	−0.348	−1.669	−0.075	−0.394	3	0.01	0.97	0.74	1.00	0	0	1	3	Succeed
18		−0.400	−0.929	−0.348	−1.669	−0.075	−0.394	3	0.01	0.97	0.74	1.00	0	0	1	3	Succeed
19		−0.400	−0.929	−0.348	−1.669	1.845	−0.394	3	0.00	0.93	1.00	0.14	0	0	1	3	Succeed
20		2.564	−1.841	−0.277	0.849	0.304	−0.394	2	0.91	0.00	0.86	1.00	0	1	0	2	Succeed
21		2.564	−1.170	−0.391	0.849	−1.229	−0.394	1	0.99	0.00	0.00	1.00	1	0	0	1	Succeed
22		2.564	−1.170	−0.391	0.849	−0.463	−0.394	1	0.72	0.00	0.25	1.00	1	0	0	1	Succeed
23		2.564	−1.170	−0.391	0.849	0.304	−0.394	2	0.04	0.00	0.98	1.00	0	1	0	2	Succeed
24	Saleem et al.	−0.400	−0.893	−0.545	0.849	−0.463	2.496	3	1.00	0.89	0.99	0.01	0	0	1	3	Succeed
25	[33]	−0.400	−0.893	−0.545	0.849	−0.463	2.496	3	1.00	0.89	0.99	0.01	0	0	1	3	Succeed
26		−0.400	−0.929	−0.348	−1.669	1.845	−0.394	3	0.00	0.93	1.00	0.14	0	0	1	3	Succeed
27		−0.400	−0.929	−0.348	0.129	−1.170	−0.394	2	0.38	0.70	0.01	1.00	0	0	0	0	Not
28		−0.400	−0.929	−0.348	0.129	−1.170	−0.394	2	0.38	0.70	0.01	1.00	0	0	0	0	Not
29		−0.400	−0.929	−0.348	0.129	−0.344	−0.394	3	0.01	0.62	0.73	1.00	0	0	1	3	Succeed
30		−0.400	−0.929	−0.348	0.129	−0.344	−0.394	3	0.01	0.62	0.73	1.00	0	0	1	3	Succeed
31		−0.400	−0.382	−0.434	−1.669	1.845	−0.394	3	0.00	1.00	1.00	0.01	0	0	1	3	Succeed
32		−0.400	−0.382	−0.434	−1.669	1.845	−0.394	3	0.00	1.00	1.00	0.01	0	0	1	3	Succeed
33		−0.400	−0.382	−0.434	0.129	−1.170	−0.394	3	0.01	0.99	0.06	1.00	0	0	1	3	Succeed
34		−0.400	−0.382	−0.434	0.129	−1.170	−0.394	3	0.01	0.99	0.06	1.00	0	0	1	3	Succeed
35		−0.400	−0.382	−0.434	0.129	−0.344	−0.394	3	0.00	0.98	0.94	1.00	0	0	1	3	Succeed
36		−0.400	−0.382	−0.434	0.129	−0.344	−0.394	3	0.00	0.98	0.94	1.00	0	0	1	3	Succeed
37		−0.400	0.347	−0.352	−1.669	−0.075	−0.394	3	0.00	1.00	0.99	0.81	0	0	1	3	Succeed
38		−0.400	0.347	−0.352	−1.669	−0.075	−0.394	3	0.00	1.00	0.99	0.81	0	0	1	3	Succeed
39		−0.400	0.347	−0.352	−1.669	1.845	−0.394	3	0.00	1.00	1.00	0.00	0	0	1	3	Succeed
40		−0.400	0.347	−0.352	−1.669	1.845	−0.394	3	0.00	1.00	1.00	0.00	0	0	1	3	Succeed
41		−0.400	0.347	−0.352	0.129	−1.170	−0.394	3	0.00	1.00	0.28	1.00	0	0	1	3	Succeed
42		−0.400	0.347	−0.352	0.129	−1.170	−0.394	3	0.00	1.00	0.28	1.00	0	0	1	3	Succeed
43		−0.400	0.347	−0.352	0.129	−0.344	−0.394	3	0.00	1.00	0.99	0.97	0	0	1	3	Succeed
44	Saleem et al.	−0.400	0.347	−0.352	0.129	−0.344	−0.394	3	0.00	1.00	0.99	0.97	0	0	1	3	Succeed
45	[35]	−0.400	−1.841	−0.282	0.849	−1.229	−0.394	1	0.99	0.00	0.00	1.00	1	0	0	1	Succeed
46		−0.400	−1.841	−0.428	0.849	−0.463	−0.394	2	0.22	0.00	0.19	1.00	0	1	0	2	Succeed
47		−0.400	−1.841	−0.282	0.849	0.304	−0.394	2	0.05	0.00	0.96	1.00	0	1	0	2	Succeed
48		−0.400	−1.367	−0.428	0.849	−1.229	−0.394	1	0.56	0.07	0.01	1.00	1	0	0	1	Succeed
49		−0.400	−1.367	−0.428	0.849	−0.463	−0.394	2	0.02	0.05	0.47	1.00	0	1	0	2	Succeed
50		−0.400	−1.367	−0.428	0.849	0.304	−0.394	2	0.00	0.04	0.99	1.00	0	1	0	2	Succeed
51		−0.400	−0.893	−0.282	0.849	−1.229	−0.394	1	0.51	0.40	0.01	1.00	1	0	0	1	Succeed
52		−0.400	−0.893	−0.428	0.849	−0.463	−0.394	2	0.00	0.45	0.77	1.00	0	0	1	3	Succeed
53		−0.400	−0.893	−0.282	0.849	0.304	−0.394	3	0.00	0.26	1.00	1.00	0	1	1	3	Succeed
54		2.564	−1.841	−0.277	0.849	−1.229	−0.394	1	1.00	0.00	0.00	1.00	1	0	0	1	Succeed
55		2.564	−1.841	−0.277	0.849	−0.463	−0.394	1	1.00	0.00	0.04	1.00	1	0	0	1	Succeed
56	Bai et al.	2.564	−0.499	−0.391	0.849	−1.229	−0.394	1	0.80	0.00	0.01	1.00	1	0	0	1	Succeed
57	[61]	2.564	−0.499	−0.391	0.849	−0.463	−0.394	2	0.07	0.00	0.68	1.00	0	1	0	2	Succeed
58		2.564	−0.499	−0.391	0.849	0.304	−0.394	2	0.00	0.00	1.00	1.00	0	1	0	2	Succeed
59		−0.400	−0.893	−0.545	0.849	−1.229	2.496	3	1.00	0.92	0.34	0.34	0	0	1	3	Succeed
60		−0.400	−0.893	−0.545	0.849	−1.229	2.496	3	1.00	0.92	0.34	0.34	0	0	1	3	Succeed
61	Ispir [40]	−0.400	−0.893	−0.545	0.849	0.304	2.496	3	1.00	0.85	1.00	0.00	0	0	1	3	Succeed
62		−0.400	−0.893	−0.545	0.849	0.304	2.496	3	1.00	0.85	1.00	0.00	0	0	1	3	Succeed
63		−0.400	−0.893	−0.693	0.849	−1.229	1.190	1	1.00	0.89	0.17	1.00	1	0	0	1	Succeed
64	Bai et al.	−0.400	−0.893	−0.693	0.849	−1.229	1.190	1	1.00	0.89	0.17	1.00	1	0	0	1	Succeed
65	[30]	−0.400	−0.893	−0.693	0.849	−0.463	1.190	3	0.87	0.85	0.97	0.95	0	0	1	3	Succeed
66		−0.400	−0.893	−0.693	0.849	−0.463	1.190	3	0.87	0.85	0.97	0.95	0	0	1	3	Succeed
67		−0.400	−0.893	−0.693	0.849	0.304	1.190	3	0.10	0.81	1.00	0.21	0	0	1	3	Succeed
68		−0.400	−0.893	−0.693	0.849	0.304	1.190	3	0.10	0.81	1.00	0.21	0	0	1	3	Succeed
69		2.564	−0.499	−0.411	0.849	−1.229	3.505	1	1.00	0.00	0.41	1.00	1	0	0	1	Succeed
70		2.564	−0.499	−0.411	0.849	−1.229	3.505	1	1.00	0.00	0.41	1.00	1	0	0	1	Succeed
71		2.564	−0.499	−0.411	0.849	−0.463	3.505	2	1.00	0.00	0.99	0.78	0	1	0	2	Succeed

(*continued on next page*)

Table 6 (*continued*)

No	Author	Scaled Inputs (Eq. (10)						Type	Layer 1 (Eqs. 15–16)				Layer 2 (Eqs. 17–18)			Model	Marked
		h (mm)	$2r_c/b$ (mm/mm)	$f_c^{'}$ (MPa)	ε_{fu} (mm/mm)	$E_f^* n_f t_f$	$\rho_{is}^* f_{yh}$		v1	v2	v3	v4	y1	y2	y3		
72		2.564	−0.499	−0.411	0.849	−0.463	3.505	2	1.00	0.00	0.99	0.78	0	1	0	2	Succeed
73		2.564	−0.499	−0.411	0.849	0.304	3.505	3	1.00	0.00	1.00	0.05	0	0	1	3	Succeed
74		2.564	−0.499	−0.411	0.849	0.304	3.505	3	1.00	0.00	1.00	0.05	0	0	1	3	Succeed
75		2.564	−0.499	−0.680	0.849	−1.229	1.744	1	1.00	0.00	0.19	1.00	1	0	0	1	Succeed
76		2.564	−0.499	−0.680	0.849	−1.229	1.744	1	1.00	0.00	0.19	1.00	1	0	0	1	Succeed
77	Dai et al.	2.564	−0.499	−0.680	0.849	−0.463	1.744	2	1.00	0.00	0.98	1.00	0	1	0	2	Succeed
78	[29]	2.564	−0.499	−0.680	0.849	−0.463	1.744	2	1.00	0.00	0.98	1.00	0	1	0	2	Succeed
79		2.564	−0.499	−0.680	0.849	0.304	1.744	3	1.00	0.00	1.00	1.00	0	1	0	2	Not
80		2.564	−0.499	−0.680	0.849	0.304	1.744	3	1.00	0.00	1.00	1.00	0	1	0	2	Not
81		−0.400	0.894	−0.381	−1.669	−0.075	−0.394	3	0.00	1.00	1.00	0.15	0	0	1	3	Succeed
82		−0.400	0.894	−0.381	−1.669	1.845	−0.394	3	0.00	1.00	1.00	0.00	0	0	1	3	Succeed
83	Han et al.	−0.400	0.894	−0.381	0.129	−1.170	−0.394	3	0.00	1.00	0.66	0.99	0	0	1	3	Succeed
84	[42]	−0.400	0.894	−0.381	0.129	−1.170	−0.394	3	0.00	1.00	0.66	0.99	0	0	1	3	Succeed
85		−0.400	0.894	−0.381	0.129	−0.344	−0.394	3	0.00	1.00	1.00	0.53	0	0	1	3	Succeed
86		−0.400	0.894	−0.381	0.129	−0.344	−0.394	3	0.00	1.00	1.00	0.53	0	0	1	3	Succeed
87		−0.304	0.894	0.390	−1.338	−0.092	−0.394	3	0.07	1.00	0.99	0.06	0	0	1	3	Succeed
88		−0.304	0.894	0.390	−1.338	−0.092	−0.394	3	0.07	1.00	0.99	0.06	0	0	1	3	Succeed
89		−0.304	0.894	0.390	−1.338	1.812	−0.394	3	0.00	1.00	1.00	0.00	0	0	1	3	Succeed
90		−0.304	0.894	0.390	−1.338	1.812	−0.394	3	0.00	1.00	1.00	0.00	0	0	1	3	Succeed
91		−0.304	0.894	0.390	0.424	−1.173	−0.394	3	0.81	1.00	0.23	0.98	0	0	0	0	Not
92		−0.304	0.894	0.390	0.424	−1.173	−0.394	2	0.81	1.00	0.23	0.98	0	0	0	0	Not
93		−0.304	0.894	0.390	0.424	−0.350	−0.394	3	0.05	1.00	0.99	0.30	0	0	1	3	Succeed
94		−0.304	0.894	0.390	0.424	−0.350	−0.394	3	0.05	1.00	0.99	0.30	0	0	1	3	Succeed
95		−0.304	0.894	1.103	−1.338	1.812	−0.394	3	0.21	1.00	1.00	0.00	0	0	1	3	Succeed
96		−0.304	0.894	1.103	−1.338	1.812	−0.394	3	0.21	1.00	1.00	0.00	0	0	1	3	Succeed
97		−0.400	0.894	−0.405	0.849	−0.463	−0.394	3	0.00	1.00	1.00	0.73	0	0	1	3	Succeed
98		−0.400	0.894	−0.405	0.849	0.304	−0.394	3	0.00	1.00	1.00	0.04	0	0	1	3	Succeed
99		−0.400	0.894	−0.384	1.353	−0.813	−0.394	3	0.00	1.00	0.99	0.95	0	0	1	3	Succeed
100		−0.400	0.894	−0.384	1.353	−0.813	−0.394	3	0.00	1.00	0.99	0.95	0	0	1	3	Succeed
101		−0.400	0.894	−0.384	1.353	0.370	−0.394	3	0.00	1.00	1.00	0.03	0	0	1	3	Succeed
102		−0.400	0.894	−0.384	1.353	0.370	−0.394	3	0.00	1.00	1.00	0.03	0	0	1	3	Succeed
103	Zeng et al.	−0.400	0.894	−0.384	1.353	1.553	−0.394	3	0.00	1.00	1.00	0.00	0	0	1	3	Succeed
104	[32]	−0.400	0.894	−0.384	1.353	1.553	−0.394	3	0.00	1.00	1.00	0.00	0	0	1	3	Succeed
105		−0.400	0.894	0.228	0.424	−0.761	−0.394	3	0.03	1.00	0.88	0.79	0	0	1	3	Succeed
106		−0.400	0.894	0.228	0.424	−0.761	−0.394	3	0.03	1.00	0.88	0.79	0	0	1	3	Succeed
107		−0.400	0.894	0.228	0.424	0.474	−0.394	3	0.00	1.00	1.00	0.00	0	0	1	3	Succeed
108		−0.400	0.894	0.228	0.424	0.474	−0.394	3	0.00	1.00	1.00	0.00	0	0	1	3	Succeed
109		−0.400	0.894	0.228	0.424	1.709	−0.394	3	0.00	1.00	1.00	0.00	0	0	1	3	Succeed

5. FRP hoop rupture Strain

The determination of the FRP hoop rupture strains plays an instrumental role in predicting the ultimate conditions of FRP-confined concrete. The general trend between the nominal confining pressure ($f_{lf,o}$) and the tested one ($f_{lf,a}$) is presented in Fig. 12. This demonstrates that $\varepsilon_{h,rup}$ is often smaller than the ultimate tensile strain of the fiber sheets (ε_{frp}), as discussed in many previous studies [i.e., [1–15]. This requires the use of rupture strain reduction factor ($k_{\varepsilon,frp} = \varepsilon_{h,rup}/\varepsilon_{frp}$) for calculating the actual confining pressures at the ultimate state. As the number of tests on rectangular specimens is limited compared with circular tests, the analysis in this subsection is conducted independently for different types of specimens and FRP materials.

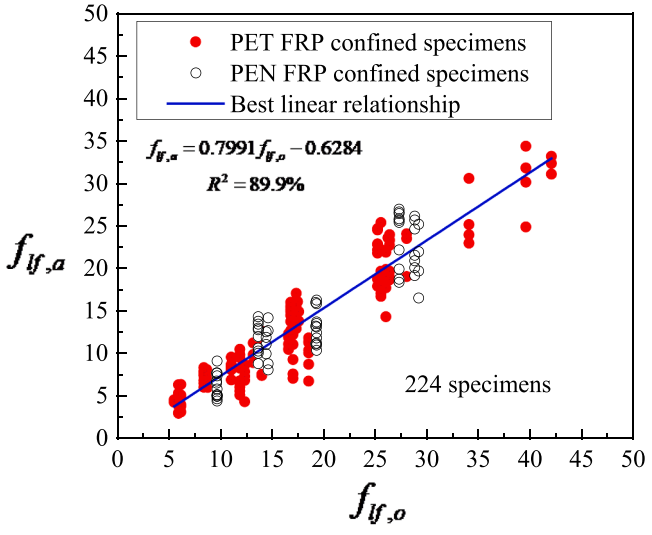

Fig. 12. Relationship between the nominal confining pressure $f_{lf,o}$ and the experimental confining pressure, $f_{lf,a}$.

According to existing literature [i.e., [18], an increase in the compressive strength of concrete has an adverse influence on the hoop rupture strain of the FRP sheets. As evident in Fig. 13 the $k_{\varepsilon,frp}$ values decrease with the increase in the $f_c^{'}$ value. In detail, the average $k_{\varepsilon,frp}$ values for PEN FRP-confined concrete in circular sections, decrease from 0.852 to 0.798 and 0.760 as the $f_{co}^{'}$ increases from the strength range of 24.1–28.6 to 31.5–33.2 MPa and 35.6–46.2 MPa. The average values of $k_{\varepsilon,frp}$ for PET FRP-confined concrete in circular sections, decrease from 0.841 to 0.813, 0.798, 0.754 and 0.661 as the $f_{co}^{'}$ increases from the strength range of 23.8–28.6 to 31.5–33.2 MPa, 35.6–39.8 MPa, 46.2–48.2 MPa and 77.6–114.9 MPa. It is also evident that an increase in the E_{frp}^* value results in a decrease in the $k_{\varepsilon,frp}$ value. Based on these observations, Eq. (19) for PEN FRP-confined tests, Eq. (20) for PET FRP confined tests, and Eq. (21) for all tests, are provided for estimating the $k_{\varepsilon,frp}$ value. It is to be noted that the results show a large variability in the $\varepsilon_{h,rup}$ values. Similar results were also reported in the literature, such as the models of Lim and Ozbakkaloglu [15] and Hany et al. [40]. Because

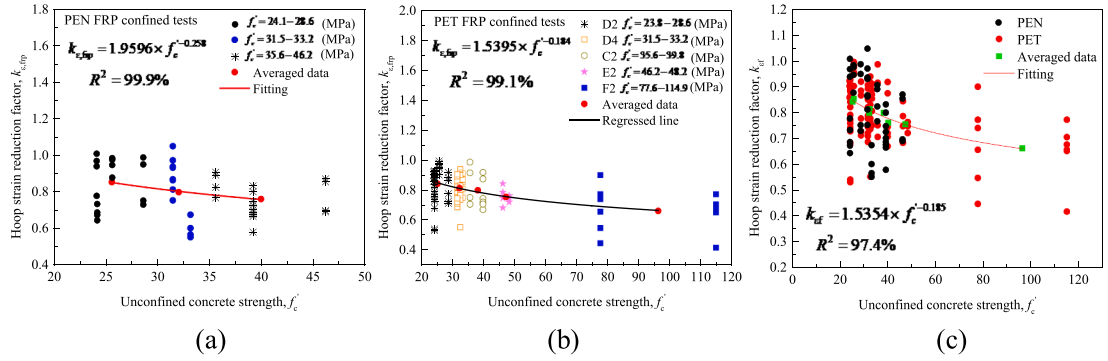

Fig. 13. Variations of $k_{\varepsilon,frp}$ against concrete strength for circular columns: (a) PEN fibers; (b) PET fibers; (c) PEN and PET fibers.

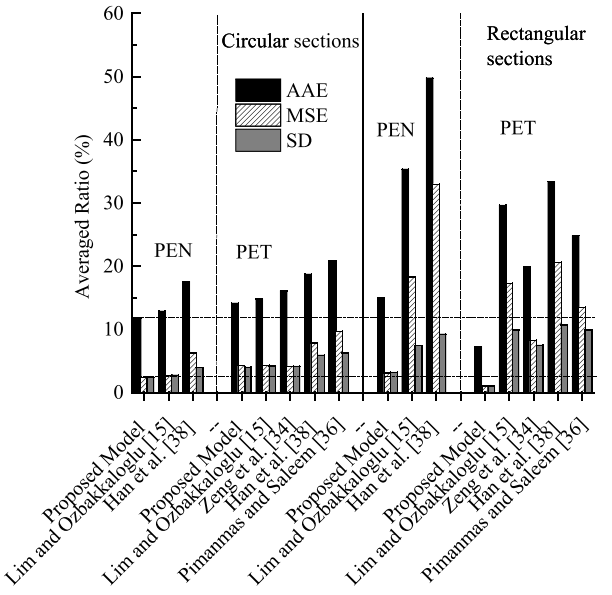

Fig. 14. Comparison between proposed and existing models of FRP strain efficiency factors.

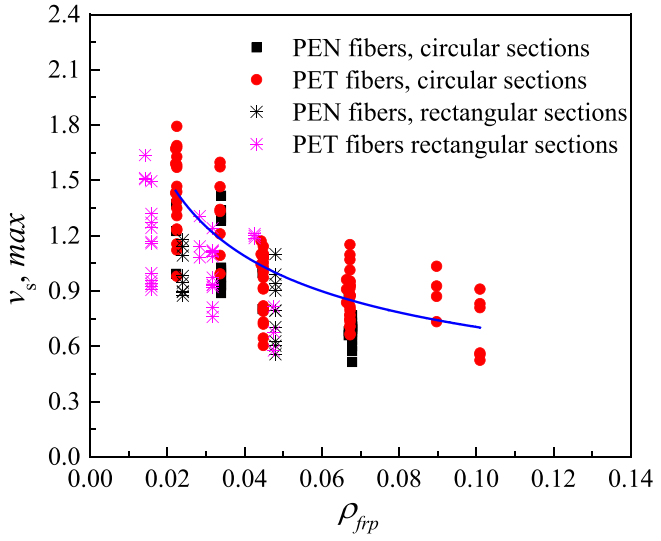

Fig. 15. Variation of maximum lateral-to-axial strain with FRP confinement ratio.

of these, the highest correlations represented by the R^2 values are obtained based on a trend from the averaged results of unconfined concrete strength for each increment selection.

$$k_{\varepsilon,frp}=\frac{\varepsilon_{h,rup}}{\varepsilon_{frp}}=1.9596\left(f_c'\right)^{-0.258} \tag{19}$$

$$k_{\varepsilon,frp}=\frac{\varepsilon_{h,rup}}{\varepsilon_{frp}}=1.5395\left(f_c'\right)^{-0.184} \tag{20}$$

$$k_{\varepsilon,frp}=\frac{\varepsilon_{h,rup}}{\varepsilon_{frp}}=1.5354\times\left(f_c'\right)^{-0.185} \tag{21}$$

For FRP-confined rectangular specimens, the next major findings were reported in the literature [i.e., [1–9,35,45]]. (1) The difference between the hoop strains recorded at the corner regions and the middle side regions of the specimen with a smaller corner radius is large due to the effect of non-uniform confining stress. As the corner radius increases, the hoop strain increases and becomes more uniformly distributed along the concrete core's perimeter; (2) The short flat side of a rectangular section exhibited greater strain than the value recorded on the long flat side; (3) Due to significant stress concentration at the corner regions, the hoop strains at these regions are smaller than those recorded at the middle regions of the cross-sections. Generally, with the presence of corner sharpness, the hoop rupture strain decreases; (4) for a certain aspect ratio and corner radius, the hoop strain at the corner regions is high for one layer compared with the results of the two or three-layered confined specimens. Based on these observations for all tested specimens and adopting the average value of hoop strain results from all strain gauges at the middle of the long sides, the short sides, and at the corners of the cross-section, Eq. (22) from tests on 62 PET FRP confined specimens only and Eq. (23) from all available 82 tests are provided for the $k_{\varepsilon,frp}$:

$$k_{\varepsilon,frp}=1-ln\left(1.35e^{\left(\frac{2r_c}{d_e}\frac{b}{h}\right)^{-0.46}}\right)\times\left(\frac{b}{h}\right)^{0.88}\left(\frac{K_{lf}}{f_c'}\right)^{0.36} \tag{22}$$

$$k_{\varepsilon,frp}=0.30\left(\frac{E_{frp}^*}{E_{co}}\right)+0.11\left(\frac{E_{frp}^*}{E_{co}}\right)^{-0.90}\left(\frac{b}{h}\right)^{-0.65}\left(\rho_{frp}\right)^{-0.19}e^{\left(\frac{2r_c}{d_e}\frac{b}{h}\right)^{1.59}} \tag{23}$$

where E_{co} is the secant modulus at the peak condition of unconfined concrete; $E_{co}=f_c'/\varepsilon_{co}$; the ε_{co} is the peak strain of unconfined concrete, which can be evaluated by the proposed Eq. (24).

$$\varepsilon_{co}=\left(-0.0054f_c'^{2.79}+42.62f_c'+1121.40\right)\times10^{-6} \tag{24}$$

The proposed FRP strain efficiency factor is compared with the existing models in Fig. 14. The horizontal axis represents the corresponding models, and the vertical axis represents the ratios of estimated errors. Three statistical indicators including the average absolute error

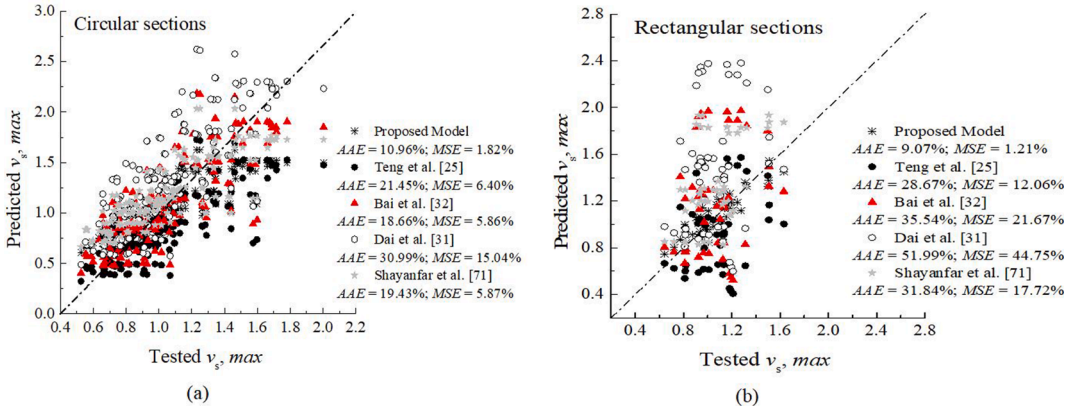

Fig. 16. Comparison between proposed and existing models of maximum lateral-to-axial strain ratios.

(*AAE*), the mean absolute error (*MSE*), and the standard deviation (*SD*) are used to assess the differences. It should be noted that the models are assessed by adopting the average value of hoop rupture strains from laboratory tests. The comparisons show that the proposed model is more accurate compared with the existing models. Furthermore, regardless of the LRS FRPs types, the estimated errors for the circular specimens are lower than those obtained for rectangular specimens.

6. Dilation behavior

6.1. Maximum Lateral-to-Axial strain, $v_{s,max}$

The ultimate secant Poisson's ratio $v_{s,max}$ plays a key role in the dilation response of FRP confined concrete, and it is required for predicting a complete axial stress–strain strain response. For this purpose, results of 182 tested specimens are used. Among the specimens, 56 and 126 specimens were rectangular and circular in their cross-sections, respectively. Test results of the specimens in terms of maximum hoop strain to axial strain ratios are provided in Fig. 15.

Tests have confirmed that LRS FRP confined concrete exhibited higher axial and lateral strains than traditional FRP confined concrete. Tests have also confirmed that the increase of the corner radius positively affects the confinement effectiveness, which effectively limits the lateral expansion of the core concrete. From the results of specimens, at an averaged PEN FRP confinement ratio of about 0.049 for the circular specimens and 0.036 for the noncircular specimens, the averaged $v_{s,max}$ values were respectively 0.899 and 0.833. Likewise, at an averaged PET FRP confinement ratio of about 0.052 for the circular specimens and 0.026 for the noncircular specimens, the averaged $v_{s,max}$ values were respectively 1.041 and 1.06. All the noncircular specimens have lower confinement ratios (on average, $\rho_{frp} = 0.031$) than those of the circular specimens (on average, $\rho_{frp} = 0.051$). However, the $v_{s,max}$ values are almost close (i.e., on average $v_{s,max} = 0.97$ for circular sections and $v_{s,max} = 0.95$). These results confirm the larger confinement stiffness leads to a lower value of hoop strain at a given axial strain for circular specimens than non-circular specimens [i.e., [35,45]. Based on a large database from the literature, Shayanfar et al. [68] have provided the following expression:

$$v_{s,max} = \frac{0.155}{\left(1.23 - 0.003 f_c'\right)\sqrt{0.5\rho_K}} \tag{25}$$

where ρ_K is the confinement stiffness index [68].

Predictions of maximum lateral-to-axial strain values by the existing models were compared with the test results of PET FRP-confined circular specimens (Fig. 16a) and rectangular specimens (Fig. 16b). It is to be noted that the assessed models were developed from the experiments of circular specimens. Besides, the models of Teng et al. [23] and Shayanfar et al. [68] were proposed based on tests with traditional FRP, whereas those provided by Dai et al. [29] and Bai et al. [30] were for LRS FRP confined concrete. Because noncircular sections exhibited larger deformations [i.e., [73], the models revealed a higher error in $v_{s,max}$ values for the rectangular specimens than for the circular specimens. For better predictions of LRS FRP confined concrete specimens, Eq. (26) for circular sections and Eq. (27) for rectangular sections are proposed.

$$v_{s,max} = \frac{0.153}{\left(0.937 - 0.0024 f_c'\right)\left(\rho_{frp}\right)^{0.535}\left(\frac{E_{frp}^*}{E_{co}}\right)^{0.255}} \tag{26}$$

$$v_{s,max} = 1.202\left(\frac{h}{b}\right)^{0.448}\left(\frac{K_{lf}}{f_c'}\right)^{-0.184} e^{\left(\frac{2r_c}{d_e}\right)^{0.520}} \tag{27}$$

Refer to Eq. (26), the expression for calculating ρ_{frp} was provided in previous discussions (i.e., Eq. (2)).

6.2. Lateral-to-Axial Strain relationship

Based on the model by Jiang and Teng [71], Dai et al. [29] firstly developed a lateral-to-axial strain relationship for LRS FRP-confined concrete. This model was improved by Bai et al. [30] using a new database. Comparisons between the existing models for lateral-axial strain relationship of circular specimens confined with conventional FRP were made by Saleem et al. [70]; their results show that the models were unable to simulate well the test results and need further modification. Compared with circular specimens, in which the concrete dilates uniformly, the concrete dilation is highly non-uniform in noncircular specimens. If the models are directly applied without considering the impact of cross-sectional shape, aspect ratio, and corner radius, the predictions may have limited accuracy.

Therefore, this subsection is to develop a model for predicting the lateral-axial strain response of LRS FRP-confined concrete specimens with circular or noncircular sections. The selected database includes tests of 126 FRP-confined concrete cylinders and 56 FRP confined square and noncircular specimens. Among the specimens, 37 cylinders had PEN FRP wraps, 89 cylinders had PET FRP wraps, 20 rectangular specimens had PEN FRP wraps, and 36 noncircular specimens had PET FRP wraps. It is to be noted that the averaged responses were considered for the same tested specimens.

Based on Eqs. (28–30) in [10], Eqs. (31 and 32) are developed in this paper respectively for LRS FRP-confined circular columns and rectangular columns,

$$\varepsilon_c = \frac{\varepsilon_l}{\nu_i\left[1 + \left(\frac{\varepsilon_l}{\nu_i \varepsilon_{co}}\right)^n\right]^{1/n}} + 0.04\varepsilon_l^{0.7}\left[1 + 21\left(\frac{f_{lf}}{f_c'}\right)^{0.80}\right] \tag{28}$$

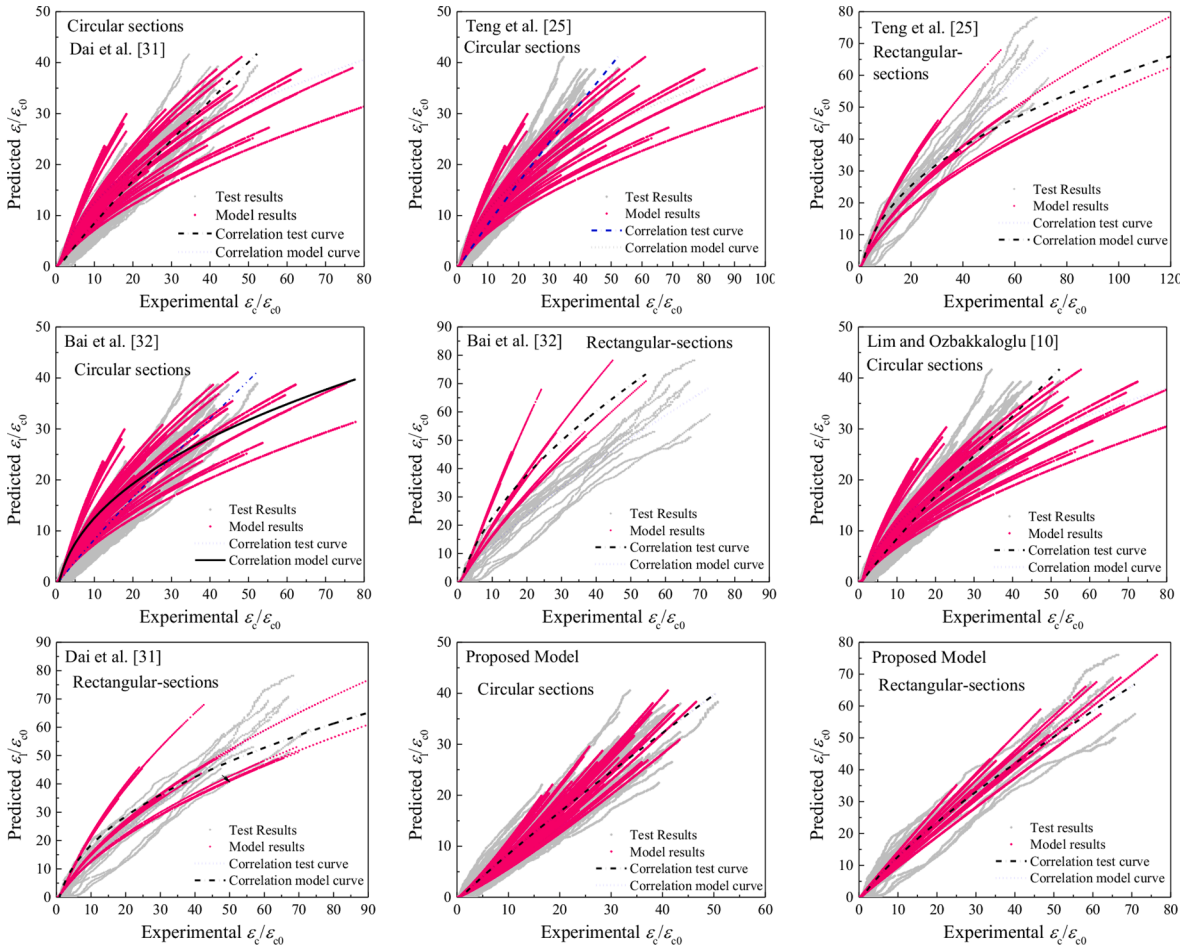

Fig. 17. Comparison between experimental and predicted lateral to axial strain response of LRS FRP-confined concrete using the proposed and existing models

$$\nu_i = 8\times10^{-6}f_c^{2} + 0.0002f_c^{'} + 0.138 \tag{29}$$

$$n = 1 + 0.03f_c^{'} \tag{30}$$

$$\varepsilon_c = \frac{\varepsilon_l}{\nu_i\left(1+\frac{\varepsilon_l}{\nu_i\varepsilon_{co}}\right)^{2.18}} + 0.40\varepsilon_l^{0.58}\left(\frac{K_{lf}\varepsilon_l}{f_c^{'}}\right)^{0.28} \tag{31}$$

$$\varepsilon_c = \left[\frac{\varepsilon_l}{\nu_i\left(1+\frac{\varepsilon_l}{\nu_i\varepsilon_{co}}\right)^{1.28}} + 0.86\varepsilon_l^{0.84}\left(\frac{K_{lf}\varepsilon_l}{f_c^{'}}\right)^{0.19}\right]\left(1+\frac{2r_c}{d_e}\right)^{-1.02} \tag{32}$$

where the termf_{lf} in Eq. (28) [10] is a variable parameter for FRP-confined concrete, which can be estimated by gradually increasing the hoop strain (ε_l) until the hoop rupture strain of the FRP jacket ($\varepsilon_{h,rup}$) is reached; ν_i is the initial Poisson's ratio of concrete and this is predicted by the same expression in Ref. [10] (Eq. (29)); the value of ε_{co} in the present model can be obtained using Eq. (24); n is defined a curve shape parameter [10]; in the present Eqs. (31 and 32), the confinement pressure is determined by $f_{lf} = K_{lf}\varepsilon_l$, where$K_{lf} = 2n_{frp}t_{frp}E^{*}_{frp}/D$for circular specimens and $K_{lf} = 2n_{frp}t_{frp}E^{*}_{frp}/d_e$for rectangular specimens.

Fig. 17 presents comparisons of the available models for both traditional FRP and LRS FRP confined concrete. Based on the correlation curves for all experimentally obtained and predicted results, it can be seen that the lateral strains in the early stage of the response are overestimated by the models. Furthermore, at a given axial strain value, these models significantly underestimated the lateral strains in the late stage of the response. On the other hand, the new expressions provided in this paper can simulate well the experimental test responses.

7. Peak stress and corresponding Strain

7.1. 1 Regression-Based approach

As before shown in Fig. 8, the stress–strain curves feature a two or three-stage response mainly depending on the FRP confinement stiffness, the cross-sectional aspect ratio, the corner radius of a cross-section, and the amount of steel hoop reinforcement. The axial stress and the axial strain at the peak condition are key requirements for the prediction of a post-peak softening response. Regression analysis of the test results with softening responses leads to the following expressions:

For LRS FRP-confined circular specimens, the peak axial stress and corresponding axial strain are determined by

$$f_{cc} = f_c^{'} + 13.47e^{\left(0.34\frac{f_{lf,o}}{f_c^{'}}\right)} \tag{33}$$

$$\varepsilon_{cc} = \varepsilon_{co} + 0.015\left(\frac{E^{*}_{frp}}{E_{co}}\right)^{2.63}\left(\rho_{frp}\right)^{1.09}e^{\left(0.13\frac{\varepsilon_{frp}}{\varepsilon_{co}}\right)} \tag{34}$$

For LRS FRP-confined rectangular specimens, the peak axial stress and corresponding axial strain are determined by

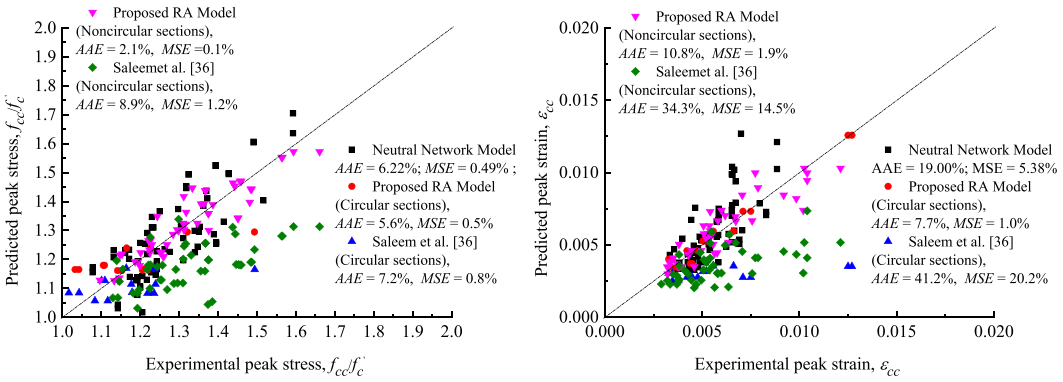

Fig. 18. Performance of the proposed and existing models of LRS FRP confined concrete: (a) Peak axial strength; (b) Peak axial strain.

$$f_{cc}=\begin{cases} f_c^{'}+164.57\left(\frac{2r_c}{d_e}\right)^{0.28}\left(\frac{b}{h}\right)^{2.14}\left[\left(\frac{E_{frp}^{*}}{E_{co}}\right)^{0.75}\left(\frac{h}{b}\right)^{2.14}\left(\rho_{frp}\right)^{0.65}+27.68\rho_{frp}\frac{E_{frp}^{*}}{E_{co}}\frac{f_{ls}}{f_c^{'}}\right];\frac{2r_c}{d_e}>0 \\ f_c^{'}\left[1+2.60\left(\frac{h}{b}\right)^{0.18}\left(\frac{E_{frp}^{*}}{E_{co}}\right)^{0.10}\left(\rho_{frp}\right)^{0.71}\right];\frac{2r_c}{d_e}=0 \end{cases} \tag{35}$$

$$\varepsilon_{cc}=\begin{cases} \varepsilon_{co}+0.075\varepsilon_{frp}\left(\frac{2r_c}{d_e}\right)^{0.66}\left(\frac{h}{b}\right)^{-0.48}\left[\left(\frac{f_{lf,o}}{f_c^{'}}\right)^{0.81}e^{\left(\frac{E_{frp}^{*}}{E_{co}}\right)^{1.70}}+14.10\frac{f_{ls}}{f_c^{'}}\right];\frac{2r_c}{d_e}>0 \\ \varepsilon_{co}+0.247\varepsilon_{frp}\left(\frac{h}{b}\right)^{1.50}\left(\frac{E_{frp}^{*}}{E_{co}}\right)^{1.61}\left(\rho_{frp}\right)^{0.67};\frac{2r_c}{d_e}=0 \end{cases} \tag{36}$$

7.2. ANN model

In this subsection, using the ANN toolbox provided in MATLAB R2020b a model was developed to estimate the axial compressive strength and strain at the peak condition of LRS FRP confined columns. The total number of data used to train, validate and test the model was 70 in total. These correspond to specimens that exhibited a three-branch response, namely flat-ascending and softening stress–strain responses. In the development processes of the ANN model, the input variables were chosen to be the same as those summarized in previous discussions of this paper (arranged as$h$or D, $C_r = 2r_c/b, f_c^{'}, \varepsilon_{frp}, n_{frp}t_{frp}E_{frp}^{*}, f_{ls}$) since they appear to have significant effects on the peak axial and corresponding strain results.

The database was randomly divided into training (70%), validation (15%), and test (15%). Using one layer of hidden nodes based on the suggestions of Ref. [65], the optimum model parameters (i.e., number of hidden nodes, learning rate) were obtained by a trial and error approach. The Levenberg-Marquardt denoted by Trainlm was selected as the training function. The performance function is MSE, and the transfer functions in both hidden and output layers are Pureline transfer functions. It is to be noted that the default transfer functions in the ANN toolbox are Tansig. By taking the log of the columns' data [Eqs. (37 and 38)] and choosing Pureline transfer functions, the model reveals an acceptable performance. Finally, the predictions from the model are practically generated following the Eqs. (39–45).

$$x=(log_{10}[x_1,x_2+1,x_3,x_4,x_5,x_6+1])^T \tag{37}$$

$$y=(log_{10}[y_1,y_2])^T \tag{38}$$

$$\left[\left(\frac{y-y_{min}}{y_{max}-y_{min}}-0.5\right)\times 2\right]=10\cdot\left[w\left(\left(\frac{x-x_{min}}{x_{max}-x_{min}}-0.5\right)\times 2\right)+a\right] \tag{39}$$

$$w=w_2\times w_1 \tag{40}$$

$$a=w_2\times b_1+b_2 \tag{41}$$

$$w_1=\begin{bmatrix} 0.7847 & -0.9068 & 0.6622 & 0.7682 & 0.7181 & -0.1080 \\ -0.6549 & -0.3637 & -1.2915 & 0.1341 & 0.7523 & 1.0755 \\ 0.2431 & 0.5106 & -0.6939 & 0.4436 & 0.5961 & 0.0783 \end{bmatrix} \tag{42}$$

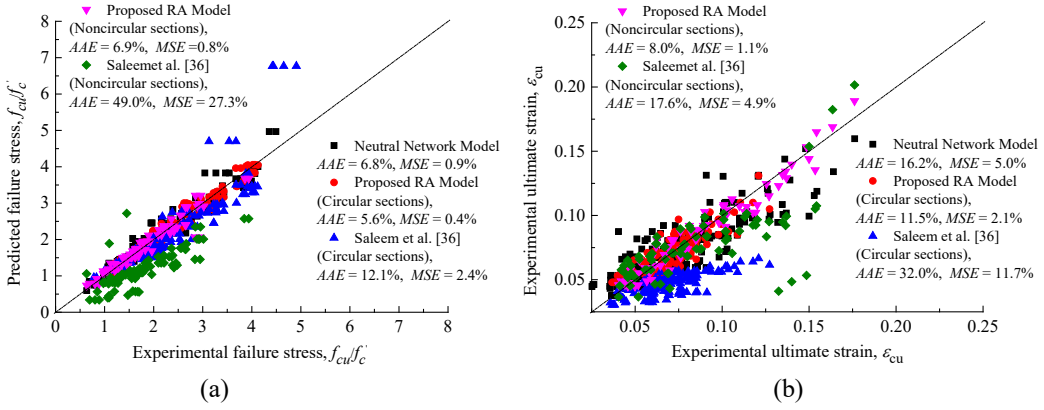

Fig. 19. Performance of the proposed and existing models of LRS FRP confined concrete: (a) Ultimate axial strength; (b) Ultimate axial strain.

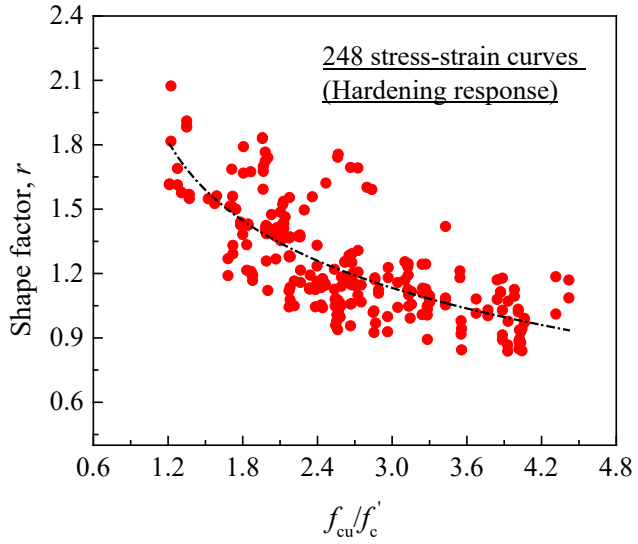

Fig. 20. Relationship between the shape factor *r*and the strength enhancement ratio $f_{cu}/f_c^{'}$.

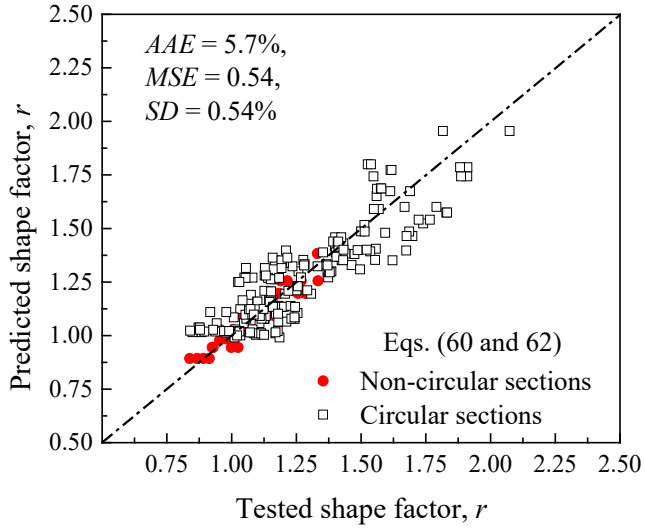

Fig. 21. Comparison between the tested and simulated shape factor.

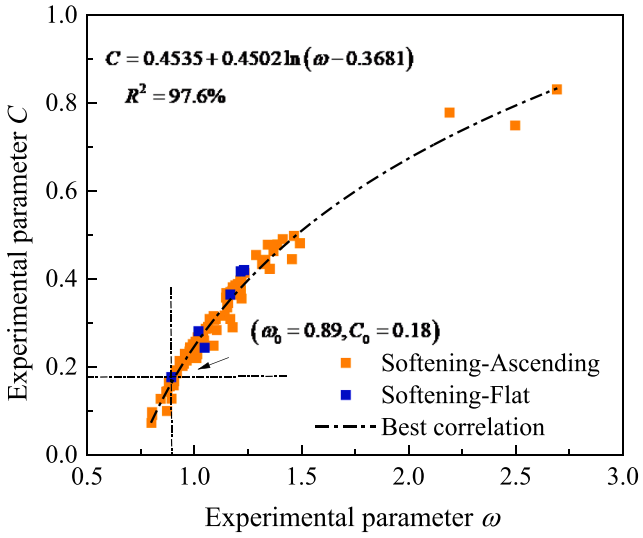

Fig. 22. Relationship between the parameters of Eq. (63): Considering the boundary conditions for a sufficiently FRP-confined concrete

$$w_2 = \begin{bmatrix} 0.0246 & 0.2479 & 0.3015 \\ -0.2268 & 0.0735 & 0.7032 \end{bmatrix} \tag{43}$$

$$b_1 = \begin{bmatrix} 0.3097 \\ -0.7181 \\ -0.8578 \end{bmatrix} \tag{44}$$

$$b_2 = \begin{bmatrix} 0.2173 \\ 0.1849 \end{bmatrix} \tag{45}$$

where *y* in Eq. (39) represents data that are now true predictions; the minimum and maximum values required for the × and *y* scaling can be found in Table 5; the terms$w_1 w_2$ b_1 and $b_2$were defined in previous discussions.

7.3. Performance of proposed peak stress and Strain models

The performance of the proposed RA and ANN (N6-3–2) models of peak axial strength and strain are verified by the database used to develop these models. Fig. 18 shows the predictions of the model as compared with the test values. Because of the unavailability of models that consider both PEN and PET FRP confinement for circular and noncircular specimens, only the model of Saleem et al. [34] was studied

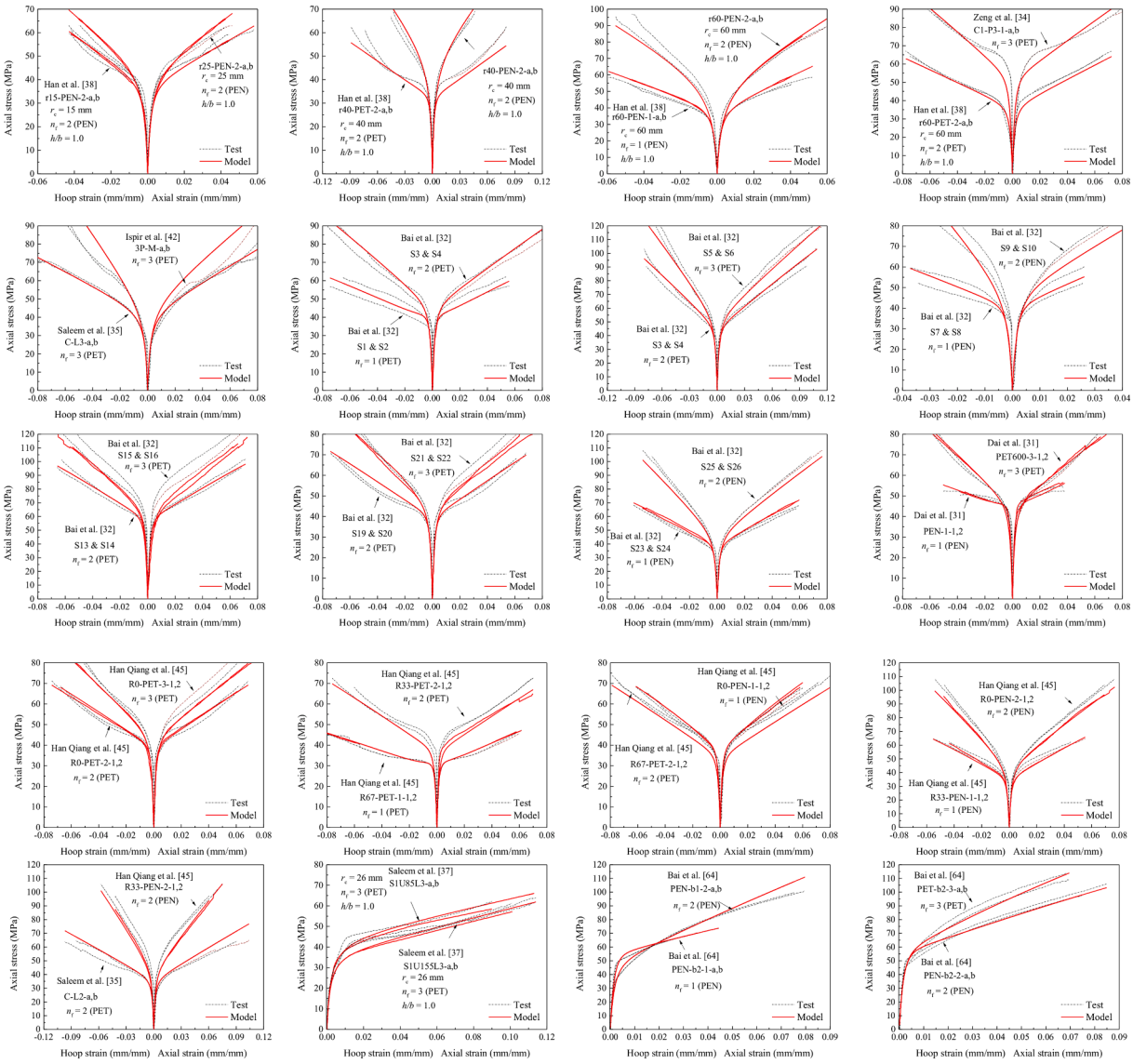

Fig. 23. Comparison between tested and predicted axial stress–strain responses.

in this verification. It is also observed that the estimated *AAE* and *MSE* errors that are given by the ANN model are almost twice those of the analytical model. The small difference in the model performance could be attributed to the difference in the analysis approach; for example, in the ANN model both the peak axial stress and strain were simulated in one analysis, whereas in RA these two predictors were independently simulated. Overall, the comparison between the predictions and the test results shows that the general errors were significantly reduced by the proposed models as compared with other methods.

8. Ultimate stress and corresponding Strain

8.1. Regression-Based approach

Similar to the previously proposed model, Eqs. (46 and 47) are proposed for the ultimate strength and corresponding strain of PET FRP confined specimens with circular sections, respectively. Also, Eqs. (48 and 49) are respectively proposed for the ultimate strength and strain of concrete confined in rectangular sections, which are applicable for PET FRP confined unreinforced and RC columns.

$$\frac{f_{cu}}{f_c'} = 0.2 + 3.93\left(\frac{f_{lf,a}}{f_c'}\right)^{0.78} \tag{46}$$

$$\frac{\varepsilon_{cu}}{\varepsilon_{co}} = 13.53 + 0.16\left(\frac{\varepsilon_{h,rup}}{\varepsilon_{co}}\right)^{1.90}\left(\rho_{frp}\right)^{0.80} e^{\left(\frac{E_{frp}^{*}}{E_{co}}\right)^{0.94}} \tag{47}$$

$$\frac{f_{cu}}{f_c'} = \begin{cases} 0.2 + 5.62\left[\left(\frac{f_{lf,a}}{f_c'}\right)^{0.76} + 0.34\left(\frac{f_{lf,a}}{f_c'}\right)\left(\frac{f_{ls}}{f_c'}\right)\right]\left(\frac{h}{b}\right)^{-0.53}\left(\frac{2r_c}{d_e}\right)^{0.18}; \frac{2r_c}{d_e} > 0 \\ 0.2 + 3.32\left(\frac{f_{lf,a}}{f_c'}\right)^{0.85}\left(\frac{h}{b}\right)^{-0.38}; \frac{2r_c}{d_e} = 0 \end{cases} \tag{48}$$

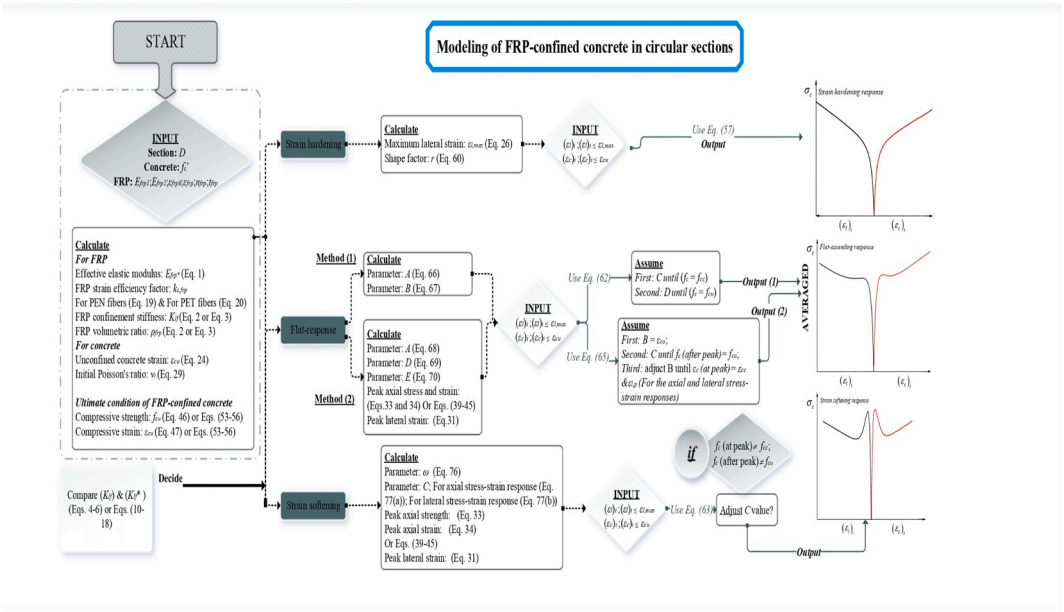

(a)

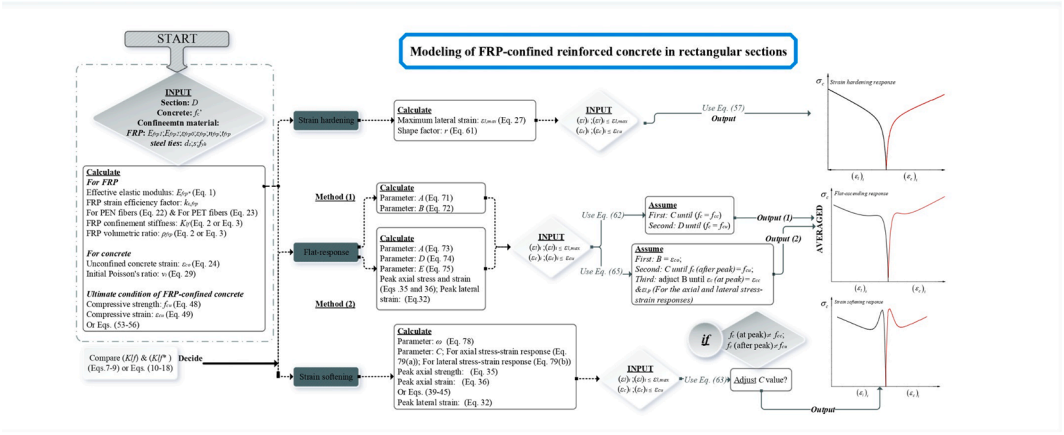

(b)

Fig. 24. Flowchart describing the generation of axial stress–strain responses of FRP-confined columns: (a) For circular columns; (b) For rectangular columns

$$\frac{\varepsilon_{cu}}{\varepsilon_{co}} = \begin{cases} 17.64 + \left[9.02\left(\rho_{frp}\right)\left(\frac{h}{b}\right)^{-0.58} e^{\left(0.16\frac{\varepsilon_{h,rup}}{\varepsilon_{co}}\right)} e^{\left(\left(\frac{E_{frp}^*}{E_{co}}\right)^{-1.30}\right)} e^{\left(\frac{2r_c}{d_e}\right)^{-4.74}} - 151.14\frac{f_{ls}}{f_c'} \right]\left(\frac{h}{b}\right)^{-0.60} ; 0 < \frac{2r_c}{d_e} \leqslant 0.25 \\ 1516.40\left(\varepsilon_{frp}\right)^{1.31}\left(\frac{f_{lf,a}}{f_c'}\right)^{0.34}\left(\frac{2r_c}{d_e}\right)^{-0.06} ; \frac{2r_c}{d_e} > 0.25 \end{cases} \quad (49)$$

where the lateral confinement pressure by the steel hoops is calculated as $f_{ls} = \rho_{ls}^* \times f_{yh}$(MPa), where f_{yh}(MPa) is the yield strength of the hoop steel reinforcement, and ρ_{ls}^* is the equivalent volumetric ratio of hoop reinforcement,

$$\rho_{ls}^* = \frac{\rho_{ls,y} b' + \rho_{ls,x} h'}{b' + h'} \quad (50)$$

$$\rho_{ls,x} = \frac{A_{ls,x}}{s b'} \quad (51)$$

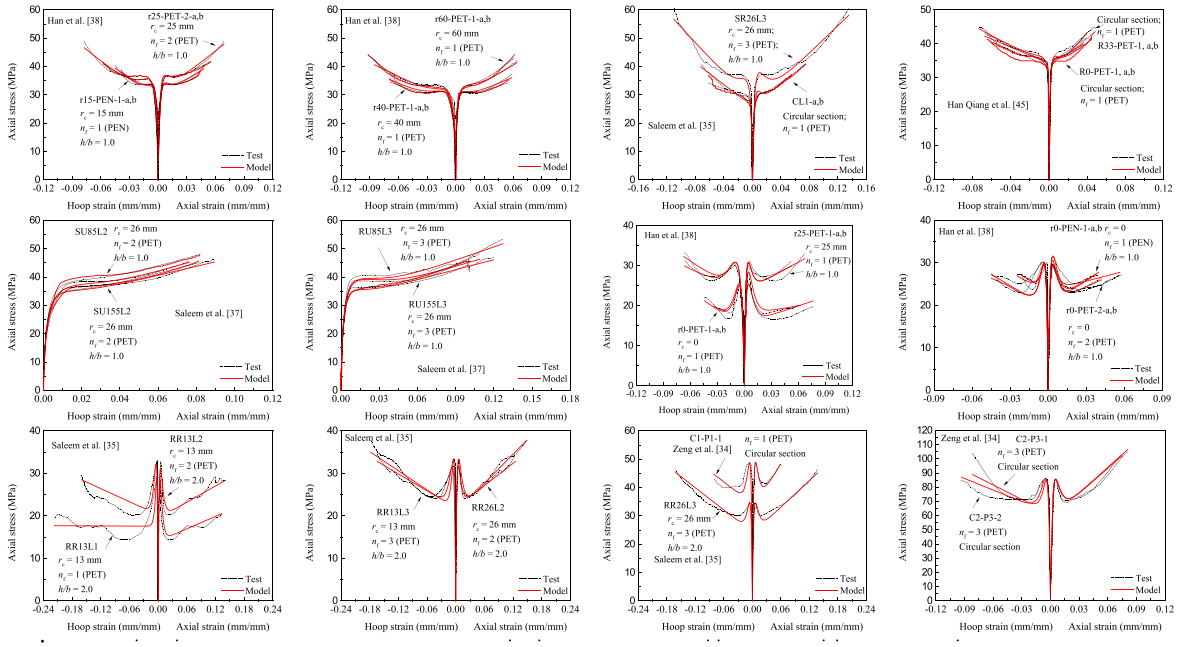

Fig. 25. Relationship between the parameters of Eq. (63): Considering the boundary conditions for a sufficiently FRP-confined concrete.

$$\rho_{ls,y} = \frac{A_{ls,y}}{sh'} \tag{52}$$

where $A_{ls,x}$ and $A_{ls,y}$(mm^2) are the cross-section areas of the reinforcement stirrups along the × and y directions (Fig. 3); s(mm) is the center-to-center spacing between the hoop reinforcing stirrups; $b'$and h'(mm) are, in the plane cross-section, the center-to-center stirrup spacing along the width and depth of a rectangular section, respectively.

8.2. ANN model

The ANN model for the ultimate compressive strength and corresponding strain of LRS FRP confined concrete columns were also developed. The algorithm and design of the present models are the same as those proposed for the peak strength and strain models. The only difference is that the number of hidden nodes that yield better results was found to be four. Besides, the number of input data is 226, which accounts for all the test specimens compiled in the present paper. Other details are as follows: network type is feed-forward backpropagation, the number of neurons for the input layer is six, the number of neurons for the output layer is two, type of backpropagation is Levenberg-Marquardt, training function is Trainlm, performance function is MSE, transfer functions in both hidden and output layers are Pureline. Using Eqs. (37–41, 53–56) and Eqs. (46–52), the predictions can be obtained.

$$w_1 = \begin{bmatrix} -0.3939 & -0.1499 & 0.5800 & -0.0839 & 0.7283 & -0.1339 \\ -0.1878 & -0.1092 & 0.3135 & -0.9725 & -1.1949 & 0.1673 \\ -0.2515 & 1.2471 & -0.5259 & -0.1079 & 0.3259 & 0.5997 \\ -0.5462 & -0.5138 & -1.0391 & -0.1742 & 0.7691 & -0.4932 \end{bmatrix} \tag{53}$$

$$w_2 = \begin{bmatrix} -0.1812 & -0.2310 & 0.3843 & 0.3471 \\ -0.2191 & -0.4140 & -0.1175 & 0.0289 \end{bmatrix} \tag{54}$$

$$b_1 = \begin{bmatrix} 0.4627 \\ 0.1836 \\ -0.3943 \\ 0.4188 \end{bmatrix} \tag{55}$$

$$b_2 = \begin{bmatrix} -0.4339 \\ 0.0517 \end{bmatrix} \tag{56}$$

8.3. Performance of proposed ultimate stress and Strain models

Fig. 19 reveals the overall performance of the proposed ultimate strength and strain expressions (Eqs. (46–52)) and those provided by Saleem et al. [34] against the test database. The N6-4–2 model proposed for the ultimate strength and its corresponding strain is also compared with the analytical predictions against the results. It is observed that the estimated *AAE* and *MSE* errors given by the regression-based model and the ANN model are almost typical for the ultimate strength, and only a slight difference in their performance is shown in the predicted ultimate strains. Besides, this evaluation reveals that the current ANN model showed almost similar accuracy to the RA model of the peak axial stress and strain.

9. Two-Stage Stress-Strain response

Using the following forms provided in Ref. [3], a two-stage response with an overall ascending branch for LRS FRP-confined circular and rectangular plain and reinforced concrete is developed based on the test results of the unreinforced and reinforced specimens in Tables 1 and 2.

$$y = \frac{Ax + Bx^2}{1 + Bx + x^r} \tag{57}$$

where$x = \varepsilon_c/\varepsilon_{co}$and y$= \sigma_c/f'_c$, ε_c and $\sigma_c$are particular levels of axial strain and stress respectively, while ε_{co} can be determined using Eq. (24). The parameter$A$, which is obtained from the boundary condition of$d\sigma_c/d\varepsilon_c = E_c$at $\varepsilon_c = 0$, can be found by substituting the resulted boundary condition into Eq. (57). The resulting expression for determining the parameter A is as follows:

$$A = \frac{E_c}{E_{co}} \tag{58}$$

where E_c is the elastic modulus of unconfined concrete (E_c=4736$\sqrt{f'_c}$) [72], and $E_{co} = f_c/\varepsilon_{co}$(MPa) is the secant modulus at the peak unconfined concrete stress.

The parameter$B$is determined from the boundary condition of$\sigma_c = f_{cu}$at$\varepsilon_c = \varepsilon_{cu}$. Upon substituting these boundary conditions into Eq. (57),

the following expression is derived:

$$B = \frac{AX - X^rY - Y}{XY - X^2} \tag{59}$$

where$X = \varepsilon_{cu}/\varepsilon_{co}andY = f_{cu}/f_c^{'}$.

In Eqs. (57) and (59), the parameter *r* is of particular importance due to its major effect on the overall shape of the stress–strain response. From a multi-parameter regression analysis of each tested stress–strain response that exhibited a two-stage response, the shape factor *r*can be obtained. Since the ultimate strength enhancement ratio$f_{cu}/f_c^{'}$ is influenced by the confinement provided by the internal hoop reinforcement and FRP wrapping jackets, as well as the geometry and dimension of the column's cross-section, there is a strong relationship between the *r*values and the$f_{cu}/f_c^{'}$ratios (see Fig. 20). The following two expressions for determining the parameter *r* are proposed for FRP-confined circular and non-circular sections, respectively. The evaluation of these expressions is provided in Fig. 21. Finally, comparisons between predictions obtained from the proposed stress–strain model with the test results of selected specimens are provided in Fig. 23.. The model simulates accurately the shape of stress–strain curves of FRP-confined unreinforced and RC columns

$$r = 0.93 + 32.43\left(\frac{E_{frp}^*}{E_{co}}\right)^{0.68} e^{\left(\frac{f_{cu}^{'}}{f_c^{'}}\right)^{-1.10}} \left(\rho_{frp}\right)^{0.56} \tag{60}$$

$$r = 0.35\left(\frac{E_{frp}^*}{E_{co}}\right)^{-0.27}\left(\frac{2r_c}{d_e}\right)^{-0.16}\left(\rho_{frp}\right)^{-0.29} - 0.36\left(\frac{f_{ls}}{f_c^{'}}\right)^{0.33} \tag{61}$$

10. Three-Stage Stress-Strain response

Zhou and Wu [73] provided a unified mathematical model that can be used to construct various constitutive relationships of concrete materials and their composite interfaces. The mathematical model has a single expression and a maximum of six parameters, whereas in most cases, three or four parameters are sufficient [i.e., *A*, *B*, *C* and *D*in Eq. (62)]. The proposed model is simple, continuous, and easy to be integrated and differentiated.

$$f(\varepsilon_c) = A\left(e^{\frac{-\varepsilon_c}{B}} + C + D\varepsilon_c\right)\left(1 - e^{\frac{-\varepsilon_c}{B}}\right) \tag{62}$$

The physical meanings of the proposed parameters are defined as: The parameter*A*controls the amplitude of the curve. The parameter-*B*quantifies the ductility and *D*determines the effect of varying confinement stiffness by its major impact on the final branch of a stress–strain curve; a $D < 0$value indicates softening confinement and $D > 0$indicates sufficient confinement. The factor *C*influences the amplitude of the overall stress–strain curve without any change in the strain axis's values.

Based on their proposed model, the following two cases are considered: (1) If a local extreme exists in Eq. (62), it can be then transformed into Eq. (63), whereε_c, ε_{cc}, and$f_{cc}$are denoted by *x*, x_0, and $f_m$in their source [73]. (2) In some special cases where more flexibility is needed for greater versatility in the curve shape, two more parameters, namely as *E* and λ (λgreater than0) can be incorporated into Eq. (62), and as a result, Eq. (64) can be applied in practice.

$$f(\varepsilon_c) = \begin{cases} \dfrac{4f_{cc}}{(1+C)^2}\left[e^{-\frac{\varepsilon_c}{\varepsilon_{cc}}ln\left(\frac{2}{1-C}\right)} + C\right]\left[1 - e^{-\frac{\varepsilon_c}{\varepsilon_{cc}}ln\left(\frac{2}{1-C}\right)}\right]; D = 0 \\ \dfrac{f_{cc}(\omega + e^{\omega} - 1)}{(1-e^{-\omega})^2(\omega + Ce^{\omega} + 1)}\left[e^{-\frac{\omega\varepsilon_c}{\varepsilon_{cc}}} + C - \dfrac{2e^{-\omega} + C - 1}{\omega + e^{\omega} - 1}\left(\dfrac{\omega\varepsilon_c}{\varepsilon_{cc}}\right)\right]; D \neq 0 \end{cases} \tag{63}$$

$$f(\varepsilon_c) = A\left(e^{-\left(\frac{\varepsilon_c}{B}\right)^E} + C + D\varepsilon_c\right)\left(1 - e^{\frac{-\varepsilon_c}{\lambda B}}\right) \tag{64}$$

where the termsω and *C*in Eq. (63) are a new set of parameters.

Based on the present analytical investigation on the specimens that exhibited, after reaching the peak stress, a slight softening region or a flat region that is finally followed by an overall ascending response, considering another expression form (Eq. (65)) gives close predictions in terms of the stress–strain curve's shape. However, the original form of Zhou and Wu [73] and the present one are both used in the analysis with resulting different expressions, and the averaged results are then adopted.

$$f(\varepsilon_c) = A\left(e^{\frac{\varepsilon_c}{B}} + C + D\varepsilon_c\right)\left(1 - e^{\frac{-\varepsilon_c}{B}}\right)^E \tag{65}$$

Using the tested stress-strain responses of LRS FRP confined concrete specimens with circular sections, the following model's parameters (i.e., Eqs. (66)–(70)) are provided. Eqs. ((66) and (67)) were obtained from Eq. (62) and Eqs. ((68)–(70)) were from Eq. (65)

$$A = 2283.54\left(\rho_{frp}\right)^{0.898}\left(\frac{E_{frp}^*}{E_{co}}\right)^{3.0}(1+C)^{-2.155}e^{\left(0.059f_c^{'}\right)} \tag{66}$$

$$B = 3.893\varepsilon_{co}\left(f_c^{'}\right)^{-0.933}\left(1 + \frac{K_{lf}}{f_c^{'}}\right)^{2.738}(1+C)^{-4.355} \tag{67}$$

$$A = 547.39\left(\rho_{frp}\right)^{0.898}\left(\frac{E_{frp}^*}{E_{co}}\right)^{3.236}(C)^{-1.014}e^{\left(0.058f_c^{'}\right)} \tag{68}$$

$$D = 1.541\left(\frac{A}{f_c^{'}}\right)^{-0.652}\left(\frac{B}{\varepsilon_{co}}\right)^{0.166}(1+C)^{0.287}\left(\frac{K_{lf}}{f_c^{'}}\right)^{0.783} \tag{69}$$

$$E = 0.346\left(1 + \frac{A}{f_c^{'}}\right)^{1.671}\left(1 + \frac{B}{\varepsilon_{co}}\right)^{-0.762} \tag{70}$$

Similarly, using the experimental results of LRS FRP confined concrete in non-circular sections, the parameters of the function are next provided. Eqs. ((71) and (72)) were obtained from Eq. (62) and Eqs. ((73)–(75)) were from Eq. (65).

$$A = 0.246f_c^{'} + 126.38\left(\frac{K_{lf}}{f_c^{'}}\right)^{0.131}(1+C)^{-2.700} + 1.288e^{\left(\frac{f_{ls}}{f_c^{'}}\right)^{0.064}} \tag{71}$$

$$B = \varepsilon_{co}\left[0.811 + \left(46.692(A)^{-0.332}(1+C)^{-2.384}\left(\frac{2r_c}{d_e}\right)^{0.324} - 1.138e^{\left(-10.348\frac{f_{ls}}{f_c^{'}}\right)}\right)\left(\frac{h}{b}\right)^{-0.252}\right] \tag{72}$$

$$A = 0.565f_c^{'} + 41.29\left(\frac{K_{lf}}{f_c^{'}}\right)^{0.370}e^{(C)^{-1.429}} + 4.44\frac{f_{ls}}{f_c^{'}} \tag{73}$$

$$B = \varepsilon_{co}\left(\frac{h}{b}\right)^{-0.815}\left[9.344\left(f_c^{'}\right)^{0.149}\left(\frac{K_{lf}}{f_c^{'}}\right)^{0.195}(C)^{-0.242}\left(\frac{2r_c}{d_e}\right)^{0.374} - 9.519e^{\left(-7.282\frac{f_{ls}}{f_c^{'}}\right)}\right] \tag{74}$$

$$E = 0.683\left(\frac{A}{f_c'}\right)^{0.729}\left(\frac{B}{\varepsilon_{co}}\right)^{-0.401} \quad (75)$$

For columns with softening response, applying a regression analysis to each curve with the use of Eq. (63), the relationship between the unknown ω & Cparameters is investigated. The correlation results are compiled in Fig. 22. Due to a slight difference in the test results, the symbols a & b in Eqs. (77 and 79) represent the results of axial and lateral stress–strain curves.

$$\omega = 0.083e^{\left(1+\frac{K_{lf}}{f_c'}\right)^{2.142}}\ e^{\left(\frac{E_{frp}^*}{E_{co}}\right)^{1.229}} \quad (76)$$

$$C = \begin{cases} 0.6295ln(\omega) + 0.2261 & (a) \\ 0.7271ln(\omega) + 0.2464 & (b) \end{cases} \quad (77)$$

$$\omega = 0.818 + 1.085\left(\frac{h}{b}\right)^{-0.965}\left(\frac{E_{frp}^*}{E_{co}}\right)(\rho_{frp})^{0.312}e^{\left(\frac{2r_c}{d_e}\right)^{2.558}}\ e^{\left(13.293\frac{f_{lx}}{f_c'}\right)} \quad (78)$$

$$C = \begin{cases} 0.6829ln(\omega) + 0.2485 & (a) \\ 0.5309 + 0.3563ln(\omega - 0.5413) & (b) \end{cases} \quad (79)$$

From Eq. (63), different types of stress–strain responses that exhibit a softening branch can be obtained based on the amount of confinement. For sufficiently confined concrete, the minimum amount of FRP confinement is also proposed for practical use (i.e., $\omega_0 = 0.89 when C_0 = 0.18$) (see Fig. 22). For ease of understanding and implementation, a step-by-step process for generating the stress–strain responses from the proposed models is shown for circular and noncircular columns in Fig. 24 (a and b). Finally, the typical three-stage relationships of LRS FRP confined concrete are predicted using the proposed expressions provided in Fig. 25, in which the model matches all different curves very well.

11. Conclusion

To capture the overall stress-strain response of larger rupture strain (LRS) FRP-confined concrete, Artificial Neural Network (ANN) models are proposed to estimate its axial compressive strength and strain, as well as to recognize its response's shape. The cross-sectional shape of circular, square, and rectangular, corner radius, number of layers of FRP wrapping jacket, and FRP material type: PEN and PET fiber sheets, and volumetric ratio of internal steel hoops were the test parameters incorporated in the models.

Besides, several RA (Regression Analytical) models to predict the full behavior of LRS FRP-confined concrete have been introduced and some of them are compared with the ANN models. For this purpose, the proposed ANN models have been successfully applied using transformed easy-to-use equations rather than using their complex computational models.

In general, the predictions of all the current models match well with the test results. They yield better results with marginal errors as compared with other existing analytical models. The ANN model that is introduced to capture the response's shape also provides better predictions as compared with the existing analytical methods. Moreover, the dilation response model based on the RA approach compared with the available models provides the best fit with the experimental results.

The models' findings are limited to the experiments investigated in this paper. More tests will increase the accuracy of these two techniques. Also, as the parameters considered by the models reveal significant effects on the overall experimental test results, additional important parameters or ranges such as the varying amount of internal steel confinement for columns with different sectional shapes and sizes are needed to check the accuracy of the models of this paper.

Declaration of Competing Interest

The authors declare that they have no known competing financial interests or personal relationships that could have appeared to influence the work reported in this paper.

Acknowledgments

The authors wish to acknowledge the financial grant supported by the National Natural Science Foundation of China (No.51978379). Moreover, the authors wish to greatly thank Dr. Hongwei Lin, Associate Professor, School of Civil Engineering, Beijing Jiaotong University, for his significant contribution in respect of reviewing and editing the manuscript.

References

[1] Wang Z, Wang D, Smith ST, Lu D. CFRP-confined square RC columns. I: experimental investigation. J Compos Constr ASCE 2012;16(2):150–60.
[2] Wang Z, Wang D, Smith ST, Lu D. CFRP-confined square RC columns. II: cyclic axial compression stress-strain model. J Compos Constr ASCE 2012;16(2):161–70.
[3] Wang Z, Wang D, Smith ST, Lu D. Experimental testing and analytical modeling of CFRP-confined large circular RC columns subjected to cyclic axial compression. Eng Struct 2012;40:64–74.
[4] Wang DY, Wang ZY, Smith ST, Yu T. Size effect on axial stress-strain behavior of CFRP-confined square concrete columns. Constr Build Mater 2016;118:116–26.
[5] Isleem HF, Wang Z, Wang D, Smith ST. Monotonic and cyclic axial compressive behavior of CFRP-confined rectangular RC columns. J Compos Constr ASCE 2018; 22(4):04018023. https://doi.org/10.1061/(ASCE)CC.1943-5614.0000860.
[6] Isleem HF, Wang DY, Wang ZY. Modeling the axial compressive stress-strain behavior of CFRP-confined rectangular RC columns under monotonic and cyclic loading. Compos Struct 2018;185(1):229–40.
[7] Isleem HF, Wang D, Wang Z. A new numerical model for polymer-confined rectangular concrete columns. Proc Inst Civ Eng Struct Build 2019;172(7):528–44. https://doi.org/10.1680/jstbu.17.00103.
[8] Isleem HF, Wang ZY, Wang DY. A new model for reinforced concrete columns strengthened with fibre reinforced polymer. Proceedings of the Institution of Civil Engineers (ICE): Structures and Buildings 2019, DOI:10.1680/jstbu.18.00159.
[9] Ozbakkaloglu T, Lim JC, Vincent T. FRP-confined concrete in circular sections: Review and assessment of stress-strain models. Eng Struct 2013;49:1068–88.
[10] Lim JC, Ozbakkaloglu T. Lateral strain-to-axial strain relationship of confined concrete. J Struct Eng 2015;141(5):04014141. https://doi.org/10.1061/(ASCE)ST.1943-541X.0001094.
[11] Lim JC, Ozbakkaloglu T. Unified stress-strain model for FRP and actively confined normal-strength and high-strength concrete. J Compos Constr ASCE 2015;19(4): 04014072. https://doi.org/10.1061/(ASCE)CC.1943-5614.0000536.
[12] Lim JC, Ozbakkaloglu T. Hoop strains in FRP-confined concrete columns: Experimental observations. Mater Struct 2015;48(9):2839–54. https://doi.org/10.1617/s11527-014-0358-8.
[13] Ozbakkaloglu T. Behavior of square and rectangular ultra high strength concrete-filled FRP tubes under axial compression. Compos Part B 2013;54:97–111.
[14] Ozbakkaloglu T, Oehlers DJ. Concrete-filled square and rectangular FRP tubes under axial compression. J Compos Constr ASCE 2008;12(4):469–77. https://doi.org/10.1061/(ASCE)1090-0268(2008)12:4(469).
[15] Lim JC, Ozbakkaloglu T. Confinement model for FRP-confined high-strength concrete. J Compos Constr ASCE 2014;18(4):04013058. https://doi.org/10.1061/(ASCE)CC.1943-5614.0000376.
[16] Fallah Pour A, Ozbakkaloglu T, Vincent T. Simplified design-oriented axial stress-strain model for FRP-confined normal- and high-strength concrete. Eng Struct 2018;175:501–16.
[17] Ozbakkaloglu T, Lim JC. Axial compressive behavior of FRP-confined concrete: Experimental test database and a new design-oriented model. Compos Part B 2013; 55:607–34.
[18] Ozbakkaloglu T, Akin E. Behavior of FRP-Confined Normal-and High-Strength Concrete under Cyclic Axial Compression. J Compos Constr 2012;16(4):451–63.
[19] Lim JC, Ozbakkaloglu T. Design model for FRP confined normal- and high-strength concrete square and rectangular columns. Mag Concr Res 2014;66(20):1020–35.
[20] Vincent T, Ozbakkaloglu T. Influence of concrete strength and confinement method on axial compressive behavior of FRP confined high- and ultra high- strength concrete. Compos Part B 2013;50:413–28.
[21] Isleem HFA. Cyclic axial behavior of rectangular RC columns strengthened with CFRP composites [M.S. thesis]. Harbin Institute of Technology: Harbin, China; 2015.
[22] Wang DY, Wang ZY, Smith ST, Yu T. Size effect on axial stress-strain behavior of CFRP confined square concrete columns. Const Build Mater 2016;118:116–26.
[23] Teng JG, Yu T, Wong YL, Dong SL. Hybrid FRP-concrete-steel tubular columns: Concept and behaviour. Constr Build Mater 2007;21(4):846–54.
[24] Ilki A, Kumbasar N. Compressive behaviour of carbon fibre composite jacketed concrete with circular and non-circular crosssections. J Earthquake Eng 2003;7(3): 381–406.

[25] Ilki A, Kumbasar N, Koc V. Low strength concrete members externally confined with FRP sheets. Struct Eng Mech 2004;18(2):167–94.
[26] Wu Y-F, Liu T, Oehlers DJ. Fundamental principles that govern retrofitting of reinforced concrete columns by steel and FRP jacketing. Adv Struct Eng 2006;9(4):507–33.
[27] Wu Y-F, Wei Y-Y. Effect of cross-sectional aspect ratio on the strength of CFRP-confined rectangular concrete columns. Eng. Struct 2010;32(1):32–45.
[28] De Luca A, Nardone F, Matta F, Nanni A, Lignola G, Prota A. Structural evaluation of full-scale FRP-confined reinforced concrete columns. J Compos Constr 2011. https://doi.org/10.1061/(ASCE)CC.1943-5614.0000152, 112-123.
[29] Dai J-G, Bai Y-L, Teng JG. Behavior and modeling of concrete confined with FRP composites of large deformability. J Compos Constr ASCE 2011;15(6):963–73.
[30] Bai Y-L, Dai J-G, Mohammadi M, Lin G, Mei S-J. Stiffness-based design oriented compressive stress-strain model for large-rupture-strain (LRS) FRP-confined concrete. Compos Struct 2019;223:110953. https://doi.org/10.1016/j.compstruct.2019.110953.
[31] Ispir M, Dalgic KD, Ilki A. Hybrid confinement of concrete through use of low and high rupture strain FRP. Compos Part B 2018;153:243–55.
[32] Zeng J-J, Ye Y-Y, Gao W-Y, Smith ST, Guo Y-C. Stress-strain behavior of polyethylene terephthalate fiber-reinforced polymer-confined normal-, high- and ultra-high-strength concrete. J Build Eng 2020;30:101243. https://doi.org/10.1016/j.jobe.2020.101243.
[33] Saleem S, Hussain Q, Pimanmas A. Compressive behavior of PET FRP-confined circular, square, and rectangular concrete columns. J Compos Constr ASCE 2017;21(3):04016097. https://doi.org/10.1061/(ASCE)CC.1943-5614.0000754.
[34] Pimanmas A, S Saleem. Evaluation of existing stress-strain models and modeling of PET FRP–confined concrete. J Mater Civ Eng 2019;31(12).10.1061/(ASCE)MT.1943-5533.0002941.
[35] Saleem S, Pimanmas A, Qureshi MI, Rattanapitikon W. Axial behavior of PETFRP-confined reinforced concrete. J Compos Constr ASCE 2021;25(1):04020079. https://doi.org/10.1061/(ASCE)CC.1943-5614.0001092.
[36] Han Q, Yuan W, Bai Y, Xiuli D. Compressive behavior of large rupture strain (LRS) FRP-confined square concrete columns: experimental study and model evaluation. Mater Struct 2020;53:99.
[37] Dai J-G, Lam L, Ueda T. Seismic retrofit of square RC columns with polyethylene terephthalate (PET) fibre reinforced polymer composites. Constr Build Mater 2012;27(1):206–17.
[38] Zeng J-J, Gao W-Y, Duan Z-J, Bai Y-L, Guo Y-C, Ouyang L-J. Axial compressive behavior of polyethylene terephthalate/carbon FRP-confined seawater sea-sand concrete in circular columns. Constr Build Mater 2020;234:117383. https://doi.org/10.1016/j.conbuildmat.2019.117383.
[39] Zeng J-J, Ye Y-Y, Guo Y-C, Lv J-F, Ouyang Yi, Jiang C. PET FRP-concrete-high strength steel hybrid solid columns with strain-hardening and ductile performance: Cyclic axial compressive behavior. Compos Part B 2020b 2020;190:107903. https://doi.org/10.1016/j.compositesb:2020.107903.
[40] Ispir M. Monotonic and cyclic compression tests on concrete confined with PET-FRP. J Compos Constr ASCE 2015;19(1):04014034. https://doi.org/10.1061/(ASCE)CC.1943-5614.0000490.
[41] Huang L, Zhang SS, Yu T, Wang ZY. Compressive behaviour of large rupture strain FRP-confined concrete-encased steel columns. Constr Build Mater 2018;183:513–22.
[42] Han Q, Yuan W-Y, Ozbakkaloglu T, Bai Y-L, Du X-L. Compressive behavior for recycled aggregate concrete confined with recycled polyethylene naphthalate/terephthalate composites. Constr Build Mater 2020;261:120498. https://doi.org/10.1016/j.conbuildmat.2020.120498.
[43] Valipour HR, Foster SJ. Nonlinear static and cyclic analysis of concrete-filled steel columns. J Const Steel Res 2010;66(6):793–802.
[44] Konstantinidis DK, Kappos AJ, Izzuddin BA. Analytical stress-strain model for high-strength concrete members under cyclic loading. J Struct Eng 2007;133(4):484–94. https://doi.org/10.1061/(ASCE)0733-9445(2007)133:4(484).
[45] Mazzoni S. Open system for earthquake engineering simulations user manual. Berkeley, CA: Univ. of California; 2003.
[46] Oreta AWC, Kawashima K. Neural network modeling of confined compressive strength and strain of circular concrete columns. J of Struct Eng 2003;129(4):554–61.
[47] Cascardi A, Micelli F, Aiello MA. An Artificial Neural Networks model for the prediction of the compressive strength of FRP-confined concrete circular columns. Eng Struct 2017;140:199–208.
[48] Elsanadedy HM, Al-Salloum YA, Abbas H, Alsayed SH. Prediction of strength parameters of FRP-confined concrete. Compos Part B 2012;43(2):228–39.
[49] Mansouri I, Ozbakkaloglu T, Kisi O, Xie T. Predicting behavior of FRP-confined concrete using neuro fuzzy, neural network, multivariate adaptive regression splines and m5 model tree techniques. Mater Struct Materiaux Constr 2016;49(10):4319–34.
[50] Mansouri I, Kisi O, Sadeghian P, Lee CH, Hu JW. Prediction of ultimate strain and strength of FRP-confined concrete cylinders using soft computing methods. Appl Sci 2017;7:751. https://doi.org/10.3390/app7080751.
[51] Ghanem1 SY, Elgazzar H. Predicting the behavior of reinforced concrete columns confined by fiber-reinforced polymers using data mining techniques. SN Appl Sci 2021;3:170. 10.1007/s42452-020-04136-5.
[52] Lim JC, Karakus M, Ozbakkaloglu T. Evaluation of ultimate conditions of FRP confined concrete columns using genetic programming. Compos Struct 2016;162:28–37.
[53] Naderpour H, Kheyroddin A, Amiri GG. Prediction of FRP-confined compressive strength of concrete using artificial neural networks. Compos Struct 2010;92(12):2817–29.
[54] Jalal M, Ramezanianpour AA. Strength enhancement modeling of concrete cylinders confined with CFRP composites using artificial neural networks. Compos Part B 2012;43(8):2990–3000.
[55] Chou J-S, Chiu C-K, Farfoura M, Al-Taharwa I. Optimizing the prediction accuracy of concrete compressive strength based on a comparison of data-mining techniques. J Comput Civ Eng 2011;25(3):242–53.
[56] Naderpour H, Kheyroddin A, Ghodrati G, Vaez H. Estimating the behavior of FRP-strengthened RC structural members using artificial neural networks. Proc Eng 2011;14:3183–90.
[57] Mohana MH. Reinforced concrete confinement coefficient estimation using soft computing models. Periodicals of Engineering and Natural Sciences 2019;7(4):1833. https://doi.org/10.21533/pen.v7i410.21533/pen.v7i4.947.
[58] Pham TM, Hadi MNS. Predicting stress and strain of FRP-confined square/rectangular columns using artificial neural networks. J Compos Constr 2014;18(6):04014019. https://doi.org/10.1061/(ASCE)CC.1943-5614.0000477.
[59] Pham TM, Hadi MNS. Strain estimation of CFRP confined concrete columns using energy approach. J Compos Constr 2013. https://doi.org/10.1061/(ASCE)CC.1943-5614.0000397, 04013001-1-04013001-11.
[60] Pham TM, Hadi MNS. Stress prediction model for FRP confined rectangular concrete columns with rounded corners. J Compos Constr 2014. https://doi.org/10.1061/(ASCE)CC.1943-5614.0000407, 04013019-1-04013019-10.
[61] Bai Y-L, Dai J-G, Teng JG. Cyclic compressive behavior of concrete confined with large rupture strain FRP composites. J Compos Constr 2014;18(1):04013025. https://doi.org/10.1061/(ASCE)CC.1943-5614.0000386.
[62] Rogers JL. Simulating structural analysis with neural network. J of Comp in Civ Eng 1994;8(2):252–65.
[63] Swingler K. Applying neural networks a practical guide. New York, London: Academic Press; 1996.
[64] Alshihri MM, Azmy AM, El-Bisy MS. Neural networks for predicting compressive strength of structural lightweight concrete. Constr Build Mater 2009;23(6):2214–9.
[65] Hornik K, Stinchcombe M, White H. Multilayer feedforward networks are universal approximators. Neural Networks 1989;2(5):359–66.
[66] Garson GD. Interpreting neural network connection weights.AI Expert, April, 47-51; 1991.
[67] Atici U. Prediction of the strength of mineral admixture concrete using multivariable regression analysis and an artificial neural network. Expert Syst Appl 2011;38(8):9609–18.
[68] Shayanfar J, Rezazadeh M, Barros JA. Analytical model to predict dilation behavior of FRP confined circular concrete columns subjected to axial compressive loading. J Compos Constr 2020;24(6):04020071. https://doi.org/10.1061/(ASCE)CC.1943-5614.0001087.
[69] Teng JG, Jiang T, Lam L, Luo YZ. Refinement of a design-oriented stress-strain model for FRP-confined concrete. J Compos Constr 2009;13(4):269–78.
[70] Saleem S, Pimanmas A, Rattanapitikon W. Lateral response of PET FRP-confined concrete. Constr Build Mater 2018;159:390–407.
[71] Jiang T, Teng JG. Analysis-oriented stress-strain models for FRP-confined concrete. Eng Struct 2007;29(11):2968–86.
[72] ACI Committee 318. Building code requirements for structural concrete (ACI 318-02) and commentary. American Concrete Institute (ACI), Farmington Hills, MI, USA; 2002.
[73] Zhou Y-W, Wu Y-F. General model for constitutive relationships of concrete and its composite structures. Compos Struct 2012;94(2):580–92.
[74] Isleem HF, Abid M, Alaloul WS, Shah MK, Zeb S, Musarat MA, et al. Axial compressive strength models of eccentrically-loaded rectangular reinforced concrete columns confined with FRP. Materials 2021;14(13):3498. https://doi.org/10.3390/ma14133498.
[75] AlAjarmeh OS, Manalo AC, Benmokrane B, Karunasena W, Mendis P. Effect of spiral spacing and concrete strength on behavior of GFRP-reinforced hollow concrete columns. J Compos Constr 2020;24(1):04019054. https://doi.org/10.1061/(ASCE)CC.1943-5614.0000987.
[76] Yang J-Q, Feng P. Analysis-oriented models for FRP confined concrete: 3D interpretation and general methodology. Eng Struct 2020;216:110749. https://doi.org/10.1016/j.engstruct.2020.110749.
[77] Jia-Qi Yang, Peng Feng. Analysis-oriented models for FRP confined high-strength concrete: 3D Interpretation of path dependency. Compos Struct 2012. In press.
[78] Lili Hu, Peng Feng, Yanran Meng, Jian Yang. Buckling behavior analysis of prestressed CFRP-reinforced steel columns via FEM and ANN. Eng Struct 2021;245:112853. https://doi.org/10.1016/j.engstruct.2021.112853.
[79] Shi Cheng, Peng Feng, Yu Bai, Lieping YE. Load-strain model for steel-concrete-FRP-concrete columns in axial compression. J Compos Construct, ASCE 2016;20(5):4016017. https://doi.org/10.1061/(ASCE)CC.1943-5614.0000664.
[80] Zheng Dang, Peng Feng, Jia-Qi Yang, Qian Zhang. Axial compressive behavior of engineered cementitious composite confined by fiber-reinforced polymer. Compos Struct 2020;243(112191). https://doi.org/10.1016/j.compstruct.2020.112191.
[81] Zeyuan Wang, Peng Feng, Yi Zhao, Tao YU. FRP-confined concrete core-encased rebar for RC columns: Concept and axial compressive behavior. Compos Struct 2019;222:110915. https://doi.org/10.1016/j.compstruct.2019.110915.
[82] Peng Feng, Shi Cheng, Yu Bai, Lieping YE. Mechanical behavior of concrete-filled square steel tube with FRP-confined concrete core subjected to axial compression. Compos Struct 2015;123(312–324). https://doi.org/10.1016/j.compstruct.2014.12.053.